EUROPEAN FUSION DEVELOPMENT AGREEMENT

EFDA–JET–PR(01)40

W.Fundamenski

Interpretation of Recent Power Width Measurements in JET MkIIGB ELMy H-modes

Interpretation of Recent Power Width Measurements in JET MkIIGB ELMy H-modes

W.Fundamenski, G.F.Matthews, V.Riccardo, P.Andrew, T.Eich[1], L.C.Ingesson[2], T.Kiviniemi[3], T.Kurki-Suonio[3], V.Philipps[1], S.Sipil‰[3], and contributors to the EFDA-JET workprogramme*

Euratom/UKAEA Fusion Association, Culham Science Centre, Abingdon, OX14 3DB, UK
[1]FZ Julich GmbH/Euratom, Institut für Plasmaphysik, TEC, D-52425 Julich, Germany
[2]FOM-Rijnhuizen, Ass. Euratom-FOM, TEC, PO Box 1207, 3430 BE Nieuwegein, NL
[3]Helsinki U. of Technology, Euratom-TEKES Assoc., PO Box 2200, FIN-02015 HUT, Finland
** See annex of J. Pamela et al, "Overview of Recent JET Results and Future Perspectives", Fusion Energy 2000 (Proc. 18th Int. Conf. Sorrento, 2000), IAEA, Vienna (2001).*

Paper to be submitted for publication in PPCF

ABSTRACT.

Results of a novel technique of measuring the deposited power profile based on thermocouples embedded in the divertor plates are presented and discussed. Power profiles were obtained for a series of 2.5MA/2.4T discharges involving a scan in the NBI heating power (4-18MW, where P_{L-H} ~5 MW) and a scan in D_2 fuelling rate (0-3×10^{22} s^{-1}). In H-mode plasmas, a narrow feature was observed in the power profile, which scaled inversely with power entering the SOL, $\lambda_{q,nw} \propto P_{SOL}^{-0.4\pm 0.1}$, while the base profile showed virtually no power dependence. At constant input power, the peak heat flux was strongly reduced by D_2 puffing (from ~20 to 4 MW/m^2), with the narrow feature in the power profile effectively suppressed. Based on numerical analysis using a guiding-centre Monte-Carlo code ASCOT, coupled to a fluid-like plasma-neutral code package OSM2/EIRENE, the above results are interpreted as a consequence of inter-ELM ion orbit loss from the pedestal region.

1. INTRODUCTION

The exhaust of power from a tokamak plasma is one of the key constraints on the design of a fusion reactor. The ITER divertor was designed on the basis of infra-red thermographic measurements of power deposition profiles in DIII-D, AUG and JT-60U, which indicate a broadening of the power profile with input power in ELMy H-mode plasmas [1, 2], the reference operating regime of ITER. Recently a novel technique was developed at JET to measure time averaged, i.e. averaged over ELMs, power profiles using thermocouples embedded in the MkIIGB divertor plates. In its original form it involved the lifting of the strike point over a junction between vertical tiles on a shot-by-shot basis and inferring the power deposition profile from the spatial derivative of the partition of energy between the two tiles [3]. Although very robust, this earlier method proved too costly in shots for general application – up to now it was only applied to one set of plasma conditions. For this reason an alternative method was developed involving the sweeping of the strike point over a thermocouple location within a single discharge and extracting the power profile using a finite-element model of the tile [4]. The new method was applied to a series of dedicated Type-I ELMy H-mode discharges comprising a scan in NBI heating power and D_2 fuelling rate; it indicates a narrowing of the power profile with increasing input power and broadening with increasing separatrix density [4]. The interpretation of this finding is the main aim of the present paper. The presentation is organized as follows: in section 2, the diagnostic methods are described; in section 3, the experimental results are presented and compared to several radial SOL transport models; in section 4, numerical modelling of the SOL plasma and ion orbit loss is discussed at length; and finally, section 5, draws conclusions about the nature of power exhaust in the recent JET experiments.

2. DESCRIPTION OF DIAGNOSTIC METHODS OF POWER DEPOSITION PROFILE MEASUREMENT

2.1 THERMOCOUPLE (TC) TECHNIQUE

The JET MkIIGB divertor is divided into 24 modules, Fig.1. In each module the tiles and the carriers are made of Carbon Fibre Composite (CFC). In most of the target tiles the weave is on the

($\theta,\perp$)-plane while in the vertical target and the dome tiles it lies on the ($\phi,\perp$)-plane. One of the directions of good conductivity is dictated by the need to promptly remove the heat from the surface subject to the plasma load. The other direction has been imposed by mechanical strength and manufacturing constraints (e.g. size, shape, accuracy). The toroidal gaps between the tiles are either 4 mm or 14 mm (usually these two alternate) and the tile thickness is adjusted so that the toroidal chamfer angle is kept constant (typically $\alpha=0.5^0$). Most of the tile rows of MkIIGB have been designed for a maximum perpendicular angle $\theta_\perp$ of 9^0, but typical operational values of $\theta_\perp$ are in the range $2\text{-}5^0$.

There are ~ 40 thermocouples embedded in the JET MkIIGB target tiles. These are mostly located in two modules (13 and 23), evenly distributed poloidally, and fitted ~10 mm below the plasma facing surface. They are sampled at a frequency of 10 Hz. In order to measure the power deposition profile on the target, the X-point is slowly lifted at a constant speed of 10-20 mm/s during the steady-state phase of the discharge (~ 6 sec), such that the entire scrape-off-layer (SOL) passes above a selected thermocouple in the vertical targets, Fig.2. In order to permit sufficient vertical displacement during the sweep, a more compact magnetic equilibrium was utilised during these experiments.

The essence of the thermocouple technique is to reconstruct the power deposition profile with the help of finite element modelling, Fig.3. This requires a construction of an accurate thermal model of the divertor tiles. The tiles are mounted onto the tile carriers such that the back of the tile is in contact with the carrier in discrete locations. In the thermal model the complex 3-D heat sink at the back of the tile (these are mounted onto the tile carriers such that the back of the tile is in contact with the carrier in discrete locations) has been simulated by fictitious convection at the back of the tile, with the heat transfer coefficient and the sink temperature, 300 W/(m^2K) and 200^0C, set to match the long term cooling of the tile. The other heat sink comes in the form of radiation from the front and side faces of the tile to the rest of the first wall, the temperature of which does not change significantly away from the strike-point during the power pulse. Consequently the radiation sink temperature has been set to 200^0C (slightly higher than the usual initial tile temperature, which varies between 170^0C and 190^0C).

The assumed power deposition profile is then varied as to minimise the difference between the measured and calculated TC traces, $T_{TC}(t)$. As in all variational techniques of this type, the functional form of the profile must be specified ab initio; as a general rule, the function should contain a minimum number of degrees of freedom consistent with matching the experimental data. Following this approach, it was found that a single exponential profile was inadequate to reproduce the full history of the measured temperature, $T_{TC}(t)$. A better fit was obtained by breaking down the power density perpendicular to the z-axis into two exponential components[4]: the wide component (q_W) with a large e-folding length (λ_W) and the thin component (q_T) with a smaller e-folding length (λ_T),

$$q(z) = q_W(z) + q_T(z) = \frac{P_{leg}/\lambda_W}{1-e^{-\frac{L}{\lambda_W}}} \frac{C\, e^{-\frac{z-z_{s-p}}{\lambda_W}}}{2\pi\, R\,(1+C)} + \frac{P_{leg}/\lambda_T}{1-e^{-\frac{L}{\lambda_T}}} \frac{e^{-\frac{z-z_{s-p}}{\lambda_T}}}{2\pi\, R\,(1+C)} \quad , \qquad (1)$$

where P_{leg} is the total power along the divertor leg, L is the poloidal length of the tile and R is the average major radius of the tile, Fig.4. C is defined as $C=P_W/P_T$, where

$$P_W = 2\pi\, R \int_0^L q_W(z)dz \qquad (2)$$

and

$$P_T = 2\pi\, R \int_0^L q_T(z)dz \,. \qquad (3)$$

The thin component, q_T, controls the peak while the wide component, q_W, determines the tail of the time derivative of the temperature, dT/dt. The above method is in good agreement with the shot-by-shot method[3] at the outer target, but not at the inner target. In order to improve the agreement at the inner target, a more physically realistic technique is required, which allows for power flow in the private flux region, for example a skewed gaussian profile (this form is suggested by observations of the electron power profile, see following section). In this case the parametrization take the form

$$q(z) = \frac{\alpha}{exp(\beta / z - 1)\, z^{\gamma}} \quad , \qquad (4)$$

where α is normalised to the deposited power

$$\alpha = P_{leg} \Big/ \left(2\pi\, R \int_0^L \frac{dz}{exp(\beta / z - 1)\, z^{\gamma}} \right). \qquad (5)$$

The width of the dT_{TC}/dt peak is linked with β, while the slow decay at the tail of the profile with γ. In general, the skewed gaussian fit gives peak heat flux values ~ 20% lower and half-widths ~ 20% larger than the double exponential; it is also in better agreement with the shape of the Langmuir probe profiles (see section 2.4). However, the skewed gaussian fit is less amenable to scale length decomposition, and for this reason the double-exponential was selected as the default fit method for the TC technique. A detailed description of thermocouple (TC) diagnostic technique for extracting power deposition profiles may be found in Ref.4.

The spatial accuracy of the reconstruction is limited by the distance of the thermocouple away from the plasma facing surface (10 mm in the case of JET MkIIGB divertor). Features smaller than 10 mm along the target can not be resolved; this corresponds to ~2.5 mm mapped to the outer-mid-plane (omp), which is of the order of the smallest λ_q observed at JET. In Type-I ELMy H-mode discharges, ELM frequencies were typically ~10 Hz which, with a strike point velocity of 10 mm/s, translates into an ELM event every 1mm-z (vertical) or 0.25 mm-omp. Since the smallest λ_q was ~3 mm-omp, the calculated profile contains ten or more ELMs per e-folding length, and thus reflects an average over these events. A consideration of various sources of error (finite distance of

thermocouple from tile surface, the effect of an empty cavity behind the thermocouple, variations in the perpendicular field line angle and flux expansion, the effect of strike point sweep velocity and finally temperature trace fitting errors) lead to an error bar estimate of ±20% on the obtained peak heat flux [4]. Comparison of the swept method against the more robust shot-by-shot technique showed agreement at the outer target to within this value [4].

2.2 TARGET LANGMUIR PROBES (LP)

In addition to the thermocouples, the MkIIGB divertor is equipped with a poloidal array of Langmuir probes (LP) which provide a measurement of the local plasma flux Γ_0 and electron temperature T_e (but not the ion temperature T_i) [5]. There are typically five poloidal probe locations per tile, with three probe tips at each poloidal location. This permits both single and triple probe modes of operation. In single mode, the probe voltage is swept at 100 Hz with a sampling rate of 10 kHz, to a maximum negative potential of -120 V. In triple mode, the probes provide measurements of Γ_0 and T_e at every sampling cycle (0.1 msec), while in single mode only once per voltage sweep cycle (10 msec). Based on standard sheath theory [6], one can estimate the electron power flux entering the sheath, and hence leaving the plasma, parallel to the magnetic field (||) as $q_{||e} \sim 5T_e\Gamma_0$. In swept strike point discharges, the electron power profile is then obtained by combining the magnetic equilibrium reconstruction with the probe signal. Typical H-mode (#50401, 12 MW NBI) profiles of plasma flux (Γ_0), electron temperature (T_e), and electron power $q_{||e}$ on the outer target are shown in Fig.5. We note the presence of vertical spikes in all three quantities, which are associated with ELM events. Since standard probe theory breaks down on the time scale of the ELM, the height of these spikes does not offer any meaningful information. On the other hand, their horizontal density, that is the number of spikes per mm-omp, is in agreement with the prediction made in the previous section (>10 ELMs per e-folding length), and suggests that ELM impact is not restricted to the vicinity of the strike point, but affects the rest of the SOL to within several e-folding lengths (the ELM deposition profile can not be extracted due to the breakdown of sheath theory). Fast infra-red measurements of ELM deposition on AUG and JET, indicate that the ELM deposition profile is only slightly broader than the inter-ELM profile. On this evidence, the ELM should not be thought of as a delta function centred on the strike point, but rather as a broad skewed gaussian profile with an extent of 1-2 λ_{SOL}. This means that the narrow feature in the total power deposition profile is unlikely to be a consequence of ELM effects alone. We will return to this point in Sec. 3.1.

The inter-ELM profile may be obtained by taking the lower envelope of the plotted LP signals. Assuming that plasma impact dominates power deposition (radiative load was estimated using tomographic reconstruction of bolometric signals, and neutral load using 2-D plasma/neutral modelling; they were found to be ~ 100 times smaller than the heat flux at the outer strike point, ~0.1 MW/m^2 vs. ~ 10 MW/m^2). One can thus infer the ion contribution to the total deposited heat flux as the difference of the total (TC) and electron (LP) powers, $q_{||i} = q_{||tot} - q_{||e}$. We will make use of this decomposition extensively in section 3.

2.3 COMPARISON OF TC AND LP MEASURED PROFILES

A comparison of the power deposition profiles on the outer target obtained by TC and LP techniques is shown in Fig.6 for two types of plasma conditions: 4 MW L-mode and 16 MW H-mode (the LP curve represents the inter-ELM electron power profile). Considering the complete independence of the two diagnostic methods, the level of agreement in profile shape is remarkable - they resemble a skewed gaussian distribution, asymmetrical with respect to the strike point. Defining the profile asymmetry factor A, as the ratio of the half-width half-maximum widths in private flux region and in the SOL, $A \equiv \lambda_{-}^{PFR}/\lambda_{-}^{SOL}$, we find $A_{LP} \sim A_{TC} \sim 0.3$. In the L-mode, the TC and LP profiles in the SOL are virtually identical, while in the H-mode, the TC heat flux is roughly four times larger than the corresponding LP measurement (the ion power profile, defined as the difference between the TC and LP profiles, would thus have a similar shape to the total profile, with a peak value of ~ 75% of the total power), but with a similar near-strike-point e-folding length. Both methods indicate that the profile becomes narrower with input power, whether expressed as the integral width ($\lambda_{int}^{L} \sim 36$ mm-z vs. $\lambda_{int}^{H} \sim 23$ mm-z) or as the full-width at half-maximum ($\lambda_{1/2}^{L} \sim 27$ mm-z vs. $\lambda_{1/2}^{H} \sim 14$ mm-z). The profiles shown in Fig.6, are representative of all the results discussed in the following section. In the remainder of the paper, profiles will be discussed only in terms of their peak values, their integral widths and their integrated powers.

The reader should be aware of a discrepancy between the TC/LP profiles and those measured by an infra-red (IR) camera on JET: the latter indicate an integral width of ~ 45 mm along the target irrespective of the power, and are fairly symmetrical about the strike point, $A_{IR} \sim 0.9$. About half of this discrepancy is attributed to the fact that the IR camera is operating close to its spatial resolution. The authors hope to investigate this effect further in the future. For the purposes of this paper, only the LP and TC data will be considered.

3. RESULTS AND ANALYSIS

During the EFDA-JET experimental campaign in june 2000, a series of discharges were dedicated to power deposition studies. They constitute a scan in: a) NBI heating power from 4 to 16 MW, b) D_2 fuelling rate into the main chamber from 0 to 3×10^{22} D/s. All experiments were performed in the same plasma configuration, with a plasma current of 2.5 MA and toroidal field on axis of 2.4 T in normal field direction ($\mathbf{B}\times\nabla\mathbf{B}\downarrow$). The total power deposition profiles were computed for each of these discharges using the TC technique, while electron heat flux profiles were obtained from the Langmuir probe closest to the chosen thermocouple in its poloidal location - since the strike point was swept, each probe gave an independent measure of the $q_{||e}$ profile. In order to combine the TC (q_{tot}) and LP ($q_{||e}$) measurements, the wall loads are expressed in terms of heat fluxes along the magnetic field lines striking the tiles ($q_{||} \sim 13 q_{surf}$), while the profiles themselves are mapped from the target to the outer mid-plane (flux expansion factor ~ 4). In order to facilitate analysis, the profiles will be expressed in terms of three variables: peak power flux $q_{||}^{peak}$, e-folding length λ_q, and integrated power per divertor leg, P_{leg}. The peak power fluxes and integrated powers are broken

down into the wide (W) and thin (T) exponential components, $q_{||tot} = q_{||W} + q_{||T}$, otherwise referred to as the base profile and the narrow layer, Fig.4. Finally, in order to capture double exponential features, when these are present, we define e-folding lengths over two different radial segments away from the separatrix (5 and 15 mm-omp), as well as the integral power width defined as $\lambda_q^{int} = \int q_{||} dr / q_{||}^{peak}$.

Before considering the dependence of the various profile quantities on heating power or gas fuelling, one preliminary observation is in order. In L-mode discharges, the heat flux decayed exponentially away from the strike point with a single e-folding length, while in H-mode, a double exponential structure appeared on the outer target only, with a narrow e-folding length near the separatrix (~3 mm mapped to outer mid-plane) and a broader base profile elsewhere in the scrape-off-layer (~5-7 mm-omp). In the subsequent sections the implications of the appearance of this narrow layer will be discussed in some detail.

3.1 NBI HEATING SCAN

We begin by examining the series of shots, which make up a scan in heating power with no additional gas fuelling. The effect of NBI heating on line average and separatrix densities is shown in Fig.7: the line-average electron density $<n_e>$ remains roughly constant at ~60% of the Greenwald density, while the normalized separatrix density $n_{e,sep}/<n_e>$, estimated using the OSM2/EIRENE modelling (see section 4), remains unchanged at 0.2-0.3. The peak total (TC) $q_{||tot}^{peak}$ and electron (LP) $q_{||e}^{peak}$ power fluxes, for inner and outer targets are plotted in Fig.8. Since the outer $q_{||}^{peak}$ is ~ 5 times larger than its corresponding inner value (for both total and electron heat fluxes), the following discussion will concentrate on the outer target. In L-mode, the electron and total power fluxes are nearly equal, while in H-mode $q_{||tot}^{peak}$ exceeds $q_{||e}^{peak}$ by roughly a factor of five. We will return to the variation of $q_{||tot}$ with P_{SOL} shortly.

As mentioned in section 2, the difference between the total and electron powers may be interpreted as being due to energetic ions. Based on this assumption, the peak power $q_{||tot}^{peak}$ is broken down into the ion and electron components, with $q_{||i} = q_{||tot} - q_{||e}$, Fig.9. Also plotted in Fig.9 are contributions from the base profile $q_{||W}^{peak}$ and the narrow layer $q_{||T}^{peak}$ (a single exponential was sufficient to match the inner profile, ie. $q_{||W}^{inner} = q_{||tot}^{inner}$). We notice a close correspondence between $q_{||W}^{peak}$ and $q_{||e}^{peak}$, and between $q_{||T}^{peak}$ and $q_{||i}^{peak}$, that is between the base and electron peak values, and the narrow and ion peak values. The base profile accounts for nearly all of the outer $q_{||tot}^{peak}$ in L-mode, decreasing to a third in 16 MW H-mode, Fig.10. The apparent dominance of the narrow layer in determining the H-mode peak power loading provides a strong incentive to understand the physical mechanism responsible for this feature. The breakdown of integrated powers is plotted in Fig.11; although the ratio P_{outer}/P_{SOL} remains approximately constant at 0.7, the relative contribution of the narrow layer, P_{thin}/P_{tot}, which is negligible in L-mode, increases to 0.35 in 16 MW H-mode. It is noteworthy that the sum of the integrated powers to both targets, $P_{outer} + P_{inner}$, are well balanced by the estimated power entering the SOL (the discrepancy of ~10% is within the diagnostic error)

implying that the ELM energy is deposited predominantly on the divertor targets. The ion contribution may be further quantified by introducing the effective ion temperature T_i, defined by assuming an ion sheath heat transmission coefficient [6] of 2.5, i.e. $q_{||i} = 2.5 T_i \Gamma_0$. The variation of T_i and T_e with P_{SOL} for both the inner and outer targets is shown in Fig.12. In L-mode, T_i / T_e is less than unity, while in H-mode (without additional gas fuelling) T_i exceeds T_e by a factor of 4 to 8 on the outside, and 10 to 20 on the inside, with outer T_i values approaching 300 eV. We can conclude that the ion channel becomes dominant as the power exceeds the L-H transition threshold, and this dominance, here quantified as T_i/T_e, continues to increase with NBI heating power.

Returning to Fig.8, the total outer peak flux may be seen to increase faster than linearly with power into the SOL, $q_{||tot}^{peak} \propto P_{SOL}^{1.34\pm0.1}$. A slightly better fit is obtained by re-plotting $q_{||tot}^{peak}$ vs. P_{outer}, with the resulting scaling $q_{||tot}^{peak} \propto P_{outer}^{1.42\pm0.1}$, Fig.9. In both cases, the exponent is only mildly affected by excluding the L-mode point; more L-mode data would be required to determine whether the scaling changes across the L-H transition. Since P_{outer} scales almost linearly with P_{SOL}, Fig.11, the above relations imply that the integral width scales inversely with power into the SOL, $\lambda_q^{int} \propto P_{SOL}^{-0.34\pm0.1}$ and $\lambda_q^{int} \propto P_{outer}^{-0.47\pm0.1}$. This agrees with the total power e-folding length fitted to the obtained profiles over 5 mm-omp, and bears little relation to that fitted over 15 mm-omp, Fig.13. In L-mode, the two lengths are equal indicating a single exponential profile, while in H-mode two effects can be noticed:

- the base profile remains constant at its L-mode value of ~ 6 mm-omp (this is also the width of the *inner* profiles, both LP and TC, at all power levels),
- a thin layer appears close to the separatrix ($\lambda_{q,5} < \lambda_{q,15}$) which becomes progressively narrower as the heating power increases, $\lambda_{q,5} \propto P_{SOL}^{-0.47\pm0.1}$ and $\lambda_{q,5} \propto P_{outer}^{-0.48\pm0.1}$ in rough agreement with the λ_q^{int} scaling; once again, if the L-mode point is left out the exponent changes only marginally.

In similarly defined e-folding lengths for the electron power flux profiles $q_{||e}$, a double exponential feature can be seen under most conditions. The base profiles for total and electron power are comparable in width, $\lambda_q^{tot}{}_{15} \sim \lambda_q^{e}{}_{15}$, although the latter tends to decrease with input power. The near-strike-point widths are also comparable, $\lambda_q^{tot}{}_{5} \sim \lambda_q^{e}{}_{5}$, both decreasing with input power. Since the electron power width reflects the plasma flux Γ_0 profile (which is roughly ambipolar, i.e. with equal ion and electron fluxes) with only a small contribution from the radial variation of the T_e profile, ie. $\lambda_q^{e} \sim \lambda_\Gamma$. Hence, the presence of hot ions in the incoming plasma stream would register in Γ_0 and $q_{||e}$ profiles, offering an explanation for the similarity of near-strike-point power widths ($\lambda_q^{i}{}_{5} \sim \lambda_q^{e}{}_{5}$) with a large excess of ion vs. electron peak heat fluxes ($T_i >> T_e$). In this picture, the difference between the total and electron peak power loads is not merely due to a profile effect, but is a consequence of higher energy of the incoming ions.

As reported in Ref.3, ELMs account for ~30% of the energy deposited on the tiles. This is comparable to the fraction of energy carried in the narrow layer, $P_{thin}/P_{tot} \sim 40\%$. A question may thus be raised as to whether ELMs could be directly responsible for the narrow feature in the power

deposition profile. In order for this to occur (the strike point is swept slowly enough such that there are many ELM events per e-folding length), the ELM deposition profile would have to be much narrower than the inter-ELM profile. This possibility can not be excluded, but there are two pieces of evidence (IR and LP) which suggest that ELM deposition profiles are somewhat broader than the inter-ELM equivalent. If this is indeed the case, than the ELMs can not be the cause of the narrow feature.

3.3 GAS FUELLING SCAN

We next turn to examine the effect of D_2 gas fuelling in the main chamber on power deposition profiles. Heating power was held constant at 12 MW and the additional D_2 fuelling rate was increased from 0 to 1.3 and 3.0×10^{22} D/s (as a result, the radiation increased somewhat, and P_{SOL} dropped from 7.2 to 5.6 MW); also included is a shot with C_2H_4 puffing at a rate of 1.2×10^{22} H/s. As a result of additional fuelling, the line averaged density $\langle n_e \rangle$ increased moderately from 60 to 90% of the Greenwald value, while $n_{e,sep}/\langle n_e \rangle$ rose sharply from 0.2 to 0.65, Fig.14. The analysis of the profiles for the gas puff scan are shown in Figs.15-20 in the same sequence and format as in the previous section; when combining data from both targets, the D_2 fuelling rate is used as the scan variable; otherwise, outer target quantities are plotted vs. outer strike point density as measured by the Langmuir probe closest to the upper TC location.

In Fig.15, the peak power flux is seen to be effectively reduced by gas puffing (50% drop at highest fuelling rate), despite the fact that the peak electron heat flux actually *increases* by 25%. The effect is more pronounced in the inner divertor, where plasma detaches from the target. In both cases, the total and electron peak fluxes approach a common value, with $q_{\|outer}^{peak} >> q_{\|inner}^{peak}$. Considering the composition of outer $q_{\|tot}^{peak}$, Fig.16, we find that the base profile is unaffected by gas puffing, while the narrow layer is strongly suppressed, i.e. the change in $q_{\|tot}^{peak}$ is due entirely to the five-fold reduction in $q_{\|thin}^{peak}$! The ion/narrow layer contribution to peak power is reduced sharply by gas fuelling, from ~0.58 to ~0.16, Fig.17. The suggestion that ions are responsible for the narrow layer and electrons for the base profile is given further support by the results of the fuelling scan; the correspondance, $i \leftrightarrow T$, $e \leftrightarrow W$, appears to be reinforced in the limit of strong gas puffing, $q_{\|i}^{peak} \rightarrow q_{\|T}^{peak}$; $q_{\|e}^{peak} \rightarrow q_{\|W}^{peak}$. The fraction of deposited power in the thin layer also decreases with Γ_D, P_{thin}/P_{outer} dropping from 0.3 to 0.09, Fig.18. In addition, up to 20% of the power entering the SOL is removed in the divertor as a result of the higher density. The magnitude of the reduction is comparable in both divertor legs, although the relative change is stronger on the inside: P_{inner}/P_{SOL} drops from 0.22 to 0.12, while P_{outer}/P_{SOL} is reduced from 0.66 to 0.56, a change of $0.1P_{SOL}$ or 0.6 MW in each case. Both ions and electrons are cooled as a results of the gas puff, although the effect on T_i is more pronounced, Fig.19; in the high density limit, T_e and T_i approach a common value, ~8 eV on the outside and ~5 eV on the inside targets. An interesting result is offered by comparing D_2 (1 D/e) and C_2H_4 (0.25 H/e) puffs:

- the D_2 puff is a factor of 2 more efficient at cooling the ions for the same rate of hydrogen atom injection; this is likely a consequence of larger charge-exchange reactivity $\langle\sigma v\rangle_{CX}$ of D-D vs. H-D, and larger fraction of energy removal per charge exchange collision.
- the C_2H_4 puff is more efficient at cooling the electrons, due to an increased concentration of carbon and the associated line radiation.

Otherwise, the two shots exhibit similar power deposition profiles. Finally, the double exponential structure of $q_{\|tot}(r)$ evident without additional fuelling is replaced by a single exponential following even a moderate amount of gas injection, Fig.20; in contrast, the electron profile retains a progressively narrower peak even at the highest target density. Neither the base profile width nor the electron profile 15-mm e-folding length, change significantly with gas injection, i.e. $\lambda_{tot,15} \sim \lambda_{e,15} \sim$ constant.

3.3 REGRESSION ANALYSIS OF POWER AND DENSITY SCANS

Two dimensional regression analysis of the power deposition widths was carried out with respect to both the line average electron density, n_{core} (which is also representative of the pedestal density, as observed on a wide range of JET ELMy H-mode configurations), and the separatrix density, n_{sep} (obtained from target Langmuir probes using the OSM2/EIRENE code package, and validated against empirical scalings of n_{sep} with ELM frequency [8]); the other independent variable was the power reaching the outer target. Details of the regression analysis may be found in Ref.4. The base profile, $\lambda_{q,base}$, shows no apparent power or density dependence, $\lambda_{q,base} \sim P_{outer}^{-0.02\pm0.10} n_{sep}^{0.04\pm0.10}$, while the thin component of the profile was found to scales as

$$\lambda_{q,narrow} \sim P_{outer}^{-0.52\pm0.10}\, n_{core}^{0.90\pm0.20} \sim P_{outer}^{-0.52\pm0.10}\, n_{sep}^{0.30\pm0.10}$$

The integral power width shows a similar dependence,

$$\lambda_{q,int} \sim P_{outer}^{-0.45\pm0.10}\, n_{core}^{1.20\pm0.20} \sim P_{outer}^{-0.45\pm0.10}\, n_{sep}^{0.40\pm0.10}$$

Both these scalings stand in sharp contrast to the ITER-99 H-mode expression, $\lambda_{q,int} \propto P_{SOL}^{+0.35\pm0.1}$ which indicates broadening, rather than narrowing of the profile with heating power. When applied to the reference ITER scenario [9], assuming neo-classical R and B dependence, the new scaling predicts a narrower power width ($\lambda_{q,int} \sim$ 2.2 - 4.4 mm-omp vs. 15 mm-omp with the ITER-99 scaling). It should be noted that recently a value of 5 mm-omp (more in line with the above estimates) was used for predictive B2.5/EIRENE simulations of the ITER divertor. Secondly, the increased closure and hence higher plasma/neutral density inside the throat of the ITER divertor is likely to impact the observed density scaling, further broadening the power profile.

3.4 COMPARISON WITH SOL TRANSPORT MODELS

An insight into the underlying physics of the dominant transport mechanism may be gained by comparing the results of the regression analysis of section 3.3 with predictions of various radial

transport models [4]. The power width λ_q can be related to the SOL radial heat diffusivity $\chi_\perp$ by a power law scaling, $\lambda_q \propto \chi_\perp^{\alpha}$, where $\alpha = 0.5$ in the conductively limited regime (high collisionality) and $\alpha = 0.6$ in the sheath limited regime (low collisionality)[6]. From among the several $\chi_\perp$ models selected for the comparison (constant, Bohm, gyro-Bohm, pseudo-classical, ∇T and current diffusive) the results of the regression analysis agree best with pseudo-classical and constant models, Fig.21. Specifically, the observed power scaling is best matched by the pseudo-classical family. In section 4, we will see that transport coeffiecients extracted using the onion-skin method [10] indicate neo-classical (as opposed to purely classical) transport in the vicinity of the separatrix, ie. in the narrow layer. The pseudo-classical model is likewise in agreement with the core/pedestal density dependence, but not with the separatrix density dependence which is better matched by the turbulent transport models. The observed agreement between the pedestal density dependence and the pseudo-classical model supports the hypothesis of power removal via ion orbit losses, which would occur from the steep gradient region in the edge transport barrier (ETB) between the pedestal and the separatrix, sampling the density to within several poloidal Larmor radii inboard of the separatrix. The fact that the observed in:out deposited power asymmetry is insensitive to plasma transport (Ω, L or H-mode) or to the ELM frequency and input power, but is strongly affected by the $\mathbf{B}\times\nabla\mathbf{B}$ direction (changes from 1:3 to 2:3) seems to support this claim. In the following sections, the effect of ion orbit losses on power deposition profiles will be assessed on the basis of extensive numerical modelling.

4. MODELLING AND INTERPRETATION

In the previous section, power deposition profiles were extracted using the TC/LP technique for a series of discharges: a narrow feature in outer target profile was observed in the high power H-modes, but not in the L-mode or the highest density H-mode. In the present section, we will attempt to interpret the presence/absence of this narrow feature in terms of ion orbit losses from the core periphery (edge transport barrier, ETB) region and their interaction with the edge plasma/neutrals. The interpretation will be based on sequential numerical modelling of the edge region, which is summarised in the following schematic:

Equilibrium (EFIT)

↓

Numerical Mesh (GRID2D)

↓

2D Edge plasma/neutral background (OSM2/EIRENE)

↓

3D Monte-Carlo ion orbit loss (ASCOT)

The reconstruction of the magnetic equilibrium is performed by solving the Grad-Shafranov equation constrained by diagnostic (magnetic pick-up coil) boundary conditions using the EFIT code [11]; in swept strike-point discharges, the equilibrium was reconstructed at the beginning of the sweep (t

~ 14 sec), when the separatrix intersects the upper part of the lower vertical tile. The obtained equilibrium is then used to construct an orthogonal numerical mesh with an emphasis on the edge of the plasma using the GRID2D grid generator[12]. The grid consists of three topologically distinct regions, which will be referred to from now on as:

- core periphery (closed field lines inboard of the separatrix, typically with $0.95 < \rho < 1.0$)
- scrape-off layer or SOL (open field lines outboard of the separatrix, $1.0 < \rho < 1.15$)
- private-flux region or PFR (open field lines below the separatrix, $0.95 < \rho < 1.0$)

These three regions have a common boundary at the X-point, where the poloidal **B**-field vanishes. They consist of different number of cells due to the orthogonality requirement, with the cell density largest in the high gradient regions (radially near separatrix and poloidally near the targets). Stored information includes the cylindrical (R,Z) coordinates of each cell centre, the four cell corners, three **B**-field components, poloidal flux and parallel distance to the target (X-point for core cells). With the assumption of toroidal symmetry, the 2-D (poloidal) grid is sufficient to represent the 3-D magnetic field of the tokamak.

4.1 2-D edge plasma/neutral background (OSM2/EIRENE)

The next step consists in reconstructing the plasma/neutral background in the region covered by the numerical mesh. There are several code packages which could be applied for this purpose, most of them based on fluid approximation for the plasma and stochastic simulation for the hydrogen neutrals. For the present application, the plasma side was handled using the OSM2 'onion-skin' code, which solves the Braginskii equations parallel to the **B**-field subject to the measured plasma fluxes and electron temperatures at the targets [10] (the onion skin approach relies on target constraints alone, and does not require any additional boundary conditions with the core plasma). The neutrals were treated using the EIRENE code, which follows the hydrogen molecular and atomic trajectories using the Monte-Carlo technique [13] and realistic vessel wall geometry. The two codes were coupled, and iterated until mutual convergence. The advantage of the OSM2/EIRENE code package for the present work lies in the fact that radial transport coefficients are not specified but rather arrived at as a consequence of matching the experimental target (Γ_0, T_e) profiles. Finally, the core periphery is treated in a simplified fashion, with plasma quantities (n_e, T_e, T_i) assigned directly from diagnostic measurement.

The first application of the OSM2/EIRENE code package to the shot-by-shot experiments discussed in section 3 has been already reported in Ref.14. Since this earlier analysis will be used extensively in section 4.2, it is worth reviewing its main findings:

- with the electron heat flux $q_{||}^{e}(r)$ constrained by the LP measurement (Γ_0, T_e), and the ratio of ion-to-electron power entering the SOL, P_i/P_e, adjusted to match the total heat flux $q_{||}^{tot}(r)$, a value of $P_i/P_e \sim 10$ was needed to obtain the correct peak heat flux $q_{||}^{tot}(0)$. A similar ratio was required for global power balance;

- with this P_i/P_e value, the inner $q_{||tot}^{peak}$ was greatly overestimated. In other words, the fluid approximation (Braginskii equations) could not explain the observed asymmetry in the peak heat flux ($q_{outer}^{peak}/q_{inner}^{peak} \sim 5$), suggesting the presence of strong drift related or kinetic effects;
- the predicted plasma conditions at the outer mid-plane separatrix ($n_e \sim 1\times10^{19}$ m^{-3}, $T_e \sim 80$ eV, $T_i \sim 350$ eV) indicate that $\nu^*_i << \nu^*_e$ (where the collisionality $\nu^* \equiv L_{||}/2\lambda \propto n/T^2$); in particular, $\nu^*_e \sim 20$ (collisional electrons), while $\nu^*_i < 1$ (collisionless ions), Fig.22;
- the extracted radial heat diffusivities are consistent with neo-classical levels ($\chi_{\perp i} \sim 0.2$ m^2/s) just outside the separatrix (neo-classical plateau regime is applicable for $(r/R)^{3/2} < \nu^*_b < 1$, satisfied for $\nu^*_i < 1$ used in place of the bounce collisionality ν^*_b), Fig.23.

The physical mechanism suggested in Ref.14 to explain the above findings was the loss of ion orbits from the core periphery (H-mode pedestal). Although the arguments offered in support of this suggestion have required further refinements, we believe that the initial interpretation was essentially correct.

We begin with a preliminary remark on the implication of the P_i/P_e ratio. Within the context of the plasma-fluid approximation, $P_i/P_e \sim 10$ implies ten times stronger ion than electron heat conduction/convection across the separatrix. However, we have seen that the fluid-picture is inadequate for explaining the in-out asymmetry, implying non-Maxwellian effects. Direct orbit losses are one possible effect:

- by removing energetic particles from the core periphery more or less directly to the divertor targets, they are responsible for a net radial transport of energy;
- due to a stronger **B**-field at the inner vs. the outer mid-plane, the resulting orbits are strongly asymmetrical, with the sign of the in:out asymmetry related to orbit topology and hence, the **B**×∇**B** drift direction (up vs. down);
- direct orbit loss implies nearly collisionless conditions; based on the fluid results ($\nu^*_e > 10$, $\nu^*_i \sim 1$) only ions can be lost directly, while electrons establish a collisional background;
- based on neo-classical theory, the width of the loss region should be of the order of the poloidal (ion) gyroradius, $\rho_{\theta,i} = \rho_i\times(B/B_\theta) \sim 7$ mm for a 1 keV D^+ ion at the outer-mid-plane field of 1.9 T (hence, on-axis of 2.5 T) and a safety factor q_{95} of 3.5.

As a consequence, the power crossing the separatrix in the form of orbit losses would be much greater in the ion channel, offering a kinetic interpretation of the required $P_i/P_e >> 1$ ratio.

The analysis sequence EFIT→GRID2D→OSM2/EIRENE was repeated for four other discharges, which effectively map the boundaries of the power and density scans: 50401 (12 MW, H-I; Γ_D=0, $0.65n_{GW}$), 50421 (16 MW, H-I; Γ_D=0, $0.65n_{GW}$), 50404 (12 MW, H-I; $\Gamma_D=3\times10^{22}$ s^{-1}, $0.9n_{GW}$), 50414 (4 MW, L; $\Gamma_D=0.5\text{-}1.5\times10^{22}$ s^{-1}, $0.3n_{GW}$). In all four simulations, the ratio of ion-to-electron power entering the SOL, P_i/P_e, was kept constant at unity; the effect of changing P_i/P_e on the

plasma solution can be assessed from the earlier simulation of the shot-by-shot experiments, typical of JET shot 49511 (14 MW, H-I; Γ_D=0, 0.65n_{GW}), for which P_i/P_e = 1 and 10 are compared. In Table 1, the results of the simulations are combined with diagnostic measurements and expressed in terms of plasma parameters (n_e, T_e, T_i) at three key locations (outer strike point, ρ~1.0, outer mid-plane separatrix, ρ~1.0, and outer mid-plane pedestal, ρ~0.9). The pedestal values were obtained as follows: n_e based on the LIDAR diagnostic, T_e from electron cyclotron emission, and T_i from charge exchange spectroscopy ($T_i = T_e$ was assumed in the simulation of section 4.2). The accepted practice of normalising λ by half the field-line connection length $L_{||}/2$, which is the typical definition of plasma collisionality, $\nu^* = L_{||}/2\lambda$, is poorly suited to comparing two different locations on the same field-line. If $L_{||}/2$ is replaced by $s_{||}$, the parallel distance from a given point to the closest target, then the newly defined $\nu^* = s_{||}/\lambda$ vanishes at the target. For this reason, in Table 1 the degree of collisionality is expressed directly in terms of the mean-free-path λ which, can be compared with a constant value of $L_{||}/2 \sim 50$ m, when applicable.

The six discharges considered in Table 1 can be organised into two groups:

- Group A (49511, 50401, 50421) exhibits a narrow feature in the power deposition profile (λ_5 ~ 3-4 mm-omp) and the associated high peak heat flux ($q_{||tot}^{peak} \sim$ 200-300 MW/m^2), which is markedly dominated by the ion channel, $q_{||tot}^{peak} >> q_{||e}^{peak}$.
- Group B (50404, 50414) does not contain this feature ($\lambda_5 \sim 6$ mm-omp) and has a much lower peak heat flux ($q_{||tot}^{peak} \sim$ 50-70 MW/m^2) which can be explained as largely due to thermal electrons, $q_{||tot}^{peak} \sim q_{||e}^{peak}$.

The following discussion will be based on the above grouping. We begin by examining the global power balance. In Group A, the integrated TC power P_{outer}^{TC} is 2-3 times larger than the integrated power based on the LP profile and OSM2/EIRENE modelling with $P_i/P_e \sim 1$, P_{outer}^{OSM2}; based on the two 49511 simulations, a roughly tenfold increase in the ion power into the SOL is required to achieve correct power accounting. In Group B, the agreement between P_{outer}^{TC} and P_{outer}^{OSM2} is much better, nearly perfect in the L-mode case (50414) and much improved in the high density H-mode (50404). Turning to electron temperature, Groups A and B differ mostly in the presence/ absence of the edge transport barrier ($T_{e,ped} \sim$ 1.5 vs. 0.5 keV; $T_{e,0} \sim$ 4.5 vs. 3 keV) and colder plasma in B at the outer target ($T_{e,t,outer} \sim$ 25-35 vs. 10-15 eV). The upstream separatrix temperatures are comparable ($T_{e,sep}$ ~70-110 eV) which is to be expected based on simple two-point model estimate ($T_{e,u} \propto P_{SOL}^{2/7}$) which predicts a very weak dependence of $T_{e,u}$ on the input power. The relatively high $T_{e,sep}$ for the high density H-mode (50404) is caused by a more efficient equipartition of energy between the ions and the electrons at higher density.

The difference in ion temperatures is more pronounced. In group A, at the outer target the ions are somewhat hotter than the electrons, $T_{i,t} \sim$ 40-70 eV ($T_{i,t}/T_{e,t} \sim$1.4-2) with P_i/P_e of unity, while $T_{i,t}$ ~ 280 eV ($T_{i,t}/T_{e,t} \sim 9$) with $P_i/P_e = 10$ (the strong influence of P_i/P_e can be explained in terms of the upstream ion collisionality, which is reduced from ~ 2 to ~ 0.5; as a consequence, the ions enter the

so called sheath-limited regime, in which the ion population samples the entire flux tube, allowing for only a small gradient between the upstream and target locations, 325 eV vs. 280 eV). In group B, the target ions are considerably colder (10-20 eV) and thermally coupled to the electrons, $T_{i,t,}/T_{e,t} \sim 1.1$. In both groups, the ratio of ion to electron upstream temperatures is roughly equal, $T_{i,sep}/T_{e,sep} \sim 2.3\text{-}2.6$, the notable exception being the $P_i/P_e = 10$ case when the ions are much hotter, $T_{i,sep}/T_{e,sep} \sim 4.7$.

The densities are least well correlated with the A-B grouping. The unfuelled H-mode discharges (group A) have SOL densities comparable to the pedestal density, that is $n_{e,t,outer} / n_{e,ped} \sim 1\text{-}2$ and $n_{e,sep} / n_{e,ped} \sim 0.4\text{-}0.8$ for $P_i/P_e = 1$. The target density is roughly halved in the presence of strong ion heating, $P_i/P_e = 10$, while the upstream density remains unaffected. In group B, the L-mode (50414) has lower line-average density, similar pedestal ($\rho \sim 0.9$) and separatrix ($\rho \sim 1.0$) densities and higher target density, $n_{e,t,outer} / n_{e,ped} \sim 4$. The strongly fuelled H-mode (50414) shows the most dramatic increase in density, both in absolute terms (the pedestal density is doubled, the separatrix tripled, and the target is ~7 times larger) as well as normalized to the pedestal value, $n_{e,t,outer} / n_{e,ped} \sim 6$.

Combining the density and temperature to calculate collisional mean-free-paths, we notice a clear distinction between the two groups. The pedestal mean-free-paths in group A are much longer then the separatrix connection length, $2\lambda_{ii,ped}/L_{\|} = 1 / \nu^*_{i,ped} \sim 15$, while those in group B are comparable to $L_{\|}$, $2\lambda_{ii,ped}/L_{\|} = 1 / \nu^*_{i,ped} \sim 1\text{-}1.5$. In other words, the ions in A are relatively collisionless (can complete several banana orbits before colliding with another ion) while those in B are fairly collisional (on average one collision per orbit). Since $T_e \sim T_i$ on the pedestal, the same is true of electron collisionality, $\nu^*_{e,ped}$. At the upstream separatrix, the ion mean-free-paths are reduced to ~ 30 m in group A with $P_i/P_e = 1$ (100 m with $P_i/P_e = 10$) and ~ 10 m in group B. Therefore, the upstream ions of A are only marginally collisional, $\nu^*_{i,sep} \sim 1.5$, with the effect of increased ion heating reducing their collisionality even further, $\nu^*_{i,sep} \sim 0.5$, while group B ions are likely to suffer several collisions before striking the target. Electrons are strongly collisional in both groups, $\nu^*_{e,sep} > 10$.

The two groups differ most markedly in target ion collisionality, with group A mean-free-paths on the order of a metre with $P_i/P_e = 1$, $\lambda_{ii,t,outer} \sim 0.3\text{-}1$ m, and tens of metres with $P_i/P_e = 10$, $\lambda_{ii,t,outer} \sim 60$ m, while group B mean-free-paths are two-to-three orders of magnitude smaller, $\lambda_{ii,t,outer} \sim 0.3\text{-}3$ cm. As mentioned previously, these lengths should not be compared to $L_{\|}/2$, but rather with the density scale length in the vicinity of the target, eg. the ionization mean-free-path. Once again, the electrons remain strongly collisional even in the case of $P_i/P_e = 10$, with $\lambda_{ii,t,outer} / \lambda_{ee,t,outer} \sim 100$.

We close the section with a look at ion-neutral (charge exchange, CX) collisions. The local values of collisionality, $\nu^* = s_{\|}/\lambda$, calculated based on the OSM2/EIRENE solution for JET shot 49511 with $P_i/P_e = 10$ are shown in Fig.24. We can infer that CX collisions are likely to play an important role in slowing down of orbit loss ions. These have a small local probability of suffering a collision with the background ions along any length of their trajectory, but this probability is fairly constant along the entire loss orbit in the SOL. On the other hand, the loss ions are only likely to experience charge exchange collisions in the atomic cloud in front of the divertor targets, however the local

probability of such an event is ~ 200 larger. Specifically, ν^*_{CX} reaches a value of 0.5 in front of the inner target, and is a factor of 10 smaller in the outer divertor. The relative contribution of i-i vs. CX collisions can only be assessed by proper Monte Carlo simulation.

4.2 3-D Monte-Carlo ion orbit loss (ASCOT)

The contribution of ion loss from neo-classical orbits to divertor target power load was first investigated by Chankin and McCracken using a 3-D Monte-Carlo guiding centre code ORBIT [15. The ion orbits were followed in a realistic JET magnetic geometry, with the assumption that the particles moved in a vacuum (no collisional effects). For ions originating inside the separatrix ($\rho < 1$), velocity space (energy-angle) can be subdivided into two regions, that of confined orbits (banana or passing) and lost orbits (to inner or outer target). The authors concluded that with normal $\mathbf{B}\times\nabla\mathbf{B}$ direction (towards the divertor target) ion orbits are preferentially lost to the *outer* target [15]. Their analysis is incomplete in one respect, namely in their implicit assumption that all ion orbits originate at the outer mid-plane. Although all ion orbits in the core of the plasma (banana or passing) must cross the outer mid-plane, this does not imply that other poloidal locations can be neglected when considering the source of *loss* ions; in reality, ions are scattered into the loss cone (i.e. are born on lost orbits) uniform in the poloidal angle. When ORBIT calculations were repeated assuming ion loss from the inner mid-plane, it was found that all ions were lost to the *inner* target, with a gradual transition between the two extremes at other poloidal locations, Fig.25.

After this initial exercise, the 3-D guiding-centre Monte-Carlo code ASCOT [16] was used to study ion orbit loss in more detail. ASCOT follows the ion test particles in a realistic JET magnetic, wall and divertor geometries and, because of its guiding centre nature, includes all neo-classical effects, i.e. all drift terms. Collisional effects (ion-ion, ion-neutral) are modelled using binomially distributed Monte Carlo operators with a specified plasma/neutral background. Test particles are initialized (launched) according to local values of density and temperature. There are two modes of code operation: a) trace mode: test particles are followed independently of each other, b) self-consistent mode: the density profiles are maintained by evaluating the neoclassical ambipolar radial electric field in the core self-consistently during the simulation. The former method is useful for evaluating the in/out deposition asymmetries, but provides no quantitative information on divertor heat loads; the latter is more accurate but requires far more computational time. The analysis was carried out in four stages:

- trace calculations in vacuum with realistic JET equilibria,
- trace calculations with specified pedestal profiles; a sensitivity study,
- trace calculations with realistic pedestal profiles from OSM2/EIRENE,
- self-consistent, grid based simulations, with plasma/neutral background reconstructed using OSM2/EIRENE modelling.

A reader interested in a detailed description of the ASCOT simulations may consult Ref.17.

4.2.1 Vacuum Trace Calculations

In the first instance, ASCOT trace simulations were performed in vacuum in order to validate the ORBIT results. The equilibrium selected (2.5 MA/2.4 T, JET shot 49511) was nearly identical to that used during the strike point sweep experiments. Good agreement was obtained between the two codes. By examining the topology of the orbits, the velocity-space mapping of Fig.26 can be easily explained. We begin with the fact that the physical mechanism responsible for the neo-classical (banana) orbits in a tokamak are the $\mathbf{B}\times\nabla\mathbf{B}$ and curvature drifts. Hence, the topology of loss orbits is determined by the direction of these drifts. With normal field direction ($\mathbf{B}\times\nabla\mathbf{B}\downarrow$), ions originating at the mid-planes and moving away from the targets experience an inward force and form confined orbits, Fig.26. The ions initially moving towards the target, terminate at their respective plates, except for a fraction of ions originating at the outer mid-plane which are reflected from the high field side and strike the inner target. As a result, the in/out asymmetry of orbit loss favours the *inner* target. When the toroidal field is reversed, the $\mathbf{B}\times\nabla\mathbf{B}$ and curvature drifts change sign, reversing the direction of ion motion within the orbit. Consequently, the topology of ion loss orbits is strongly modified by field reversal ($\mathbf{B}\times\nabla\mathbf{B}\uparrow$). Ions moving towards the targets are now pulled inward, towards the core of the plasma, Fig.26. The majority of these ions end up on confined orbits, with some loss occurring from the outer mid-plane, where the **B**-field is weaker. Of the ions moving away from the target, those originating at the outer mid-plane can be reflected from the high field side and strike the outer target (others terminate at the inside), while none of the ions originating at the inner mid-plane can become reflected from the low field side so as to strike the inner target. As a result, the in/out asymmetry of orbit loss strongly favours the *outer* target. It is also noteworthy that on average the orbits are roughly three times longer with $\mathbf{B}\times\nabla\mathbf{B}\uparrow$ facing away from the target, with a correspondingly higher likelihood of collisional broadening. For the above reasons, field reversal experiments could provide a valuable test to the orbit loss hypothesis.

4.2.2 Plasma Trace Calculations

As a second step, ASCOT trace simulations were performed with analytically specified plasma background (no neutrals) in order to investigate the sensitivity of the in/out asymmetry to several parameters: launch position (radial and poloidal), ion energy, plasma density and temperature, and $\mathbf{B}\times\nabla\mathbf{B}$ direction. In the default case, the ions were launched at $\rho = \rho_{ped} = 0.95$ at the outer mid-plane, deep enough to prevent direct losses from the launch location, with a monotonic energy of $1.5T_i$ where $T_{i,ped} = T_{e,ped} = 1$ keV, $n_{e,ped} = 10^{19}$ m^{-3} and $E_r = 0$. The results of the parametric scan are shown in Table 2. It can be seen that the in/out asymmetry indeed favours the inner target ($\sim$ 2.5:1 in the default case). As expected, this asymmetry is inverted dramatically with field reversal ($\mathbf{B}\times\nabla\mathbf{B}\uparrow$), with nearly all orbits terminating at the outer target. The scan in launch position indicates that orbit loss occurs in a layer of the order of the poloidal Larmor radius inboard of the separatrix ($0.99 < \rho < 1.0$); in the case of ions originating at the outer mid-plane, the in/out asymmetry reverses from 3.0 to 0.75 within this layer, as could be expected from section 4.2.1. The scan in poloidal

launch position at fixed ρ of 0.95 (outer mid-plane θ=0 vs. uniform poloidal launch θ=[0,2π]), demonstrates the effectiveness of collisions in uniformly populating the ion density as a function of the poloidal angle. The effect of changing plasma conditions at the pedestal can best be understood by plotting the results in terms of the separatrix collisionality $\nu^*_{i,sep}$, Fig.27. Although the in/out asymmetry is seen do decrease with $\nu^*_{i,sep}$, the level of collisionality required ($\nu^*_{i,sep} > 1$) to reach f_{in}/f_{out} of unity would lead to significant broadening of the deposited profiles. We can conclude that in order to match the experimental findings (narrow layer on the outer target), there must exist some mechanism capable of increasing the loss to the outer target at low collisionality.

4.2.3 Plasma/Neutrals Trace Calculations

In the next stage, trace calculations were performed with the OSM2/EIRENE plasma/neutral background for JET shot 49511 with $P_i/P_e = 10$ (see section 4.1) and compared to the vacuum case. In the default case, the ions were launched uniformly in poloidal angle on the ρ = 0.95 surface (to assure no direct losses of launch particles) with an energy of $1.5T_i$ (although mono-energetic at first, the ions quickly thermalize to a Maxwellian distribution); the $\mathbf{B}\times\nabla\mathbf{B}$ pointed towards the target and no radial electric fields were present. Four parameters were varied in the course of a parametric scan: the $\mathbf{B}\times\nabla\mathbf{B}$ direction, the ion launch energy and the radial electric fields in two regions: the pedestal and the SOL. The results are shown in Table 3. In the default case, the in/out asymmetry of ~ 2.2 was obtained, with only a small reduction due to the plasma/neutral background (f_{in}/f_{out} ~ 2.4 with no SOL). As before, field reversal leads to strong inversion of asymmetry in favour of the outer target. Within the range of energies considered, there is only a marginal effect of the ion birth energy on f_{in}/f_{out}. More significantly, the radial electric field inside the separatrix has little effect on the in-out asymmetry. Although negative (inward) **E**-fields reduce ion loss appreciably by squeezing the ion orbits, the effect is comparable for both inner and outer targets. In contrast, radial **E**-field in the SOL exerts a strong influence on the in-out asymmetry: $f_{in}/f_{out} = 5.6$ for -100 kV/m and $f_{in}/f_{out} = 0.25$ for +100 kV/m. Since, $E_r = -\nabla_r\varphi \approx -3\nabla_r T_e$ in the scrape-off layer should be positive (outward) due to the radial decay of the electron temperature (estimated at + 30 to 100 kV/m in JET high power H-modes), we expect the experimental in/out asymmetry to shift in favour of the outer target. The physical mechanism responsible for this effect is the $E_r\times B_\phi$ drift which adds a poloidal velocity component to the ion motion; with a sufficiently strong outward electric field, the ions are effectively drawn towards the outer target. Hence, the $\mathbf{E}\times\mathbf{B}$ drift appears to be a leading candidate mechanism to explain the observed narrow feature in the outer target deposition profile.

4.2.4 Plasma/Neutrals Self-Consistent Calculations

In the final modelling stage (to date), ASCOT simulations were performed in the self-consistent mode with plasma/neutral background taken from OSM2/EIRENE for JET shot 49511 with P_i/P_e = 1 and 10; as before, a case with vacuum SOL is included for comparison. The pedestal profiles were obtained directly from diagnostic data as discussed in section 4.1. For each case, simulations

were performed at different levels of the SOL radial electric field. Sufficient number of particles was launched to assure that good statistics in the calculated target deposition profiles on each target. These are shown in Figs.28-30 for the three cases (no SOL background, P_i/P_e = 1 and 10) and four values of E_r^{SOL} (0, 22.5, 45, 75 kV/m). To facilitate discussion, they are parametrized in terms of the relevant physical quantities: the peak heat flux q^{peak}[MW/m^2], integral power width λ_{int}[mm-omp], and deposited power P_{target}[MW/m]. The peak heat flux, Fig.31, shows three notable trends:

- $q_{out}^{peak}/q_{in}^{peak}$ increases monotonically with E_r^{SOL} for all three cases, reaching unity at ~ 40 kV/m and a value of 2 at ~ 70 kV/m (the peak occurs ~ 1 mm-omp below the magnetic strike point due to the downward B×∇B drift),
- q^{peak} (both inner and outer) is roughly halved due to the presence of SOL plasma/neutrals
- q^{peak} for P_i/P_e = 1 is roughly 25% lower than for P_i/P_e = 10, i.e. the background ion temperature has relatively little effect on the deposition profile.

The deposited power (MW/m) shows similar trends, Fig.32, with one difference: power to the inner target is only weakly affected by E_r^{SOL} (with SOL plasma/neutrals), while the outer target power increases monotonically with field strength. Consequently, the integral power width (mapped to the outer mid-plane) Fig.33, scales differently with E_r^{SOL} for inner and outer targets. The outer λ_{int} remains unchanged at ~ 2 mm-omp (3 mm without SOL background) while the inner λ_{int} increases with E_r^{SOL} from 4 to 6 mm-omp (5 to 8 mm without SOL). In other words, the radial **E**-field broadens the inner deposition profile with no appreciable effect on the outer target. This can be understood in terms of the interaction between the **E**×**B** and **B**×∇**B** drifts: the ions moving towards the inner target are slowed down by the additional $E_r \times B_\phi$ drift and so spend more time below the inner mid-plane where the **B**×∇**B** drift acts to pull them away from the separatrix. The ions bound for the outer target are further accelarated by the $E_r \times B_\phi$ drift, reducing the already small broadening effect of the **B**×∇**B** drift.

Aside from broadening the inner profile, the **E**×**B** ↔ **B**×∇**B** drift synergism can also shift the peak of the inner power profile away from the magnetic strike point, given sufficiently large positive radial **E**-field in the SOL, Fig.34. This mechanism offers an explanation for the observed shift of the strike point away from the separatrix during a giant ELM at the inner target, with little or no shift at the outer target [18]. During an ELM event, the pedestal **B**-field becomes ergodized leading to prompt electron loss to the divertor targets [19] (due to their smaller mass and hence higher thermal speed, electrons are able to travel much faster along the open field lines than the ions - the ions follow on the slower timescale defined by the plasma sound speed; in this respect the initial phase of an ELM event is analogous to the formation of an electrostatic sheath when a solid object is inserted into the plasma). The remaining layer of positive charge (i.e. the net ion surplus) creates a strong outward electric field in the SOL, as well as parallel fields along the field lines which limit further electron loss. Subsequent ion trajectories, assuming sufficiently ion energy to assure low collisionality, correspond to the typical ion orbit loss considered already and modelled by ASCOT,

Fig.34. They are modified by the radial **E-**field, and due to the synergistic $\mathbf{E}\times\mathbf{B} \leftrightarrow \mathbf{B}\times\nabla\mathbf{B}$ drift effect, the inner orbits are shifted outwards while the outer orbits are only mildly effected.

Let us turn to a comparison of the ASCOT simulations with the estimated values of q_i^{peak} and λ_{int} based on TC/LP analysis (section 3.3) shot 50401 (equivalent to 49511). The obtained values were 9.4 and 4.5 MW/m^2, and 3 and 6 mm-omp for the outer and inner targets, respectively. The outer peak heat flux value agrees with the ASCOT estimate for $E_r^{SOL} \sim 55$ kV/m, while the ratio of in/out asymmetry in q^{peak} is replicated for ~ 75 kV/m. Similarly, the simulated integral widths can be made to agree with the experiment for $E_r^{SOL} \sim 60$ kV/m. In fact, the simulated outer profiles are narrower than those observed experimentally. The required E_r^{SOL} value lies within the estimated range based on LP electron temperature profile, 30 to 100 kV/m. We can concluded that the orbit loss could indeed be the cause of the observed power profiles in JET high power H-modes. However, the true test of this hypothesis will require ASCOT simulations for the remaining shots in section 4.1; this work is underway and will be reported on shortly.

4.2.5 Extrapolation of power width scaling to ITER

We close the modelling section with a brief consideration of ion orbit losses in ITER. A comparison of the relevant parameters between JET (50421 with $P_i/P_e=1$) and ITER is shown in Table 4. Based on the assumption that ion separatrix collisionality is the key parameter governing ion loss from the core periphery, we would expect these to be at least as important in ITER, for which $\nu^*_{i,sep}$ is ~25% lower than the JET value (equal power to ion and electrons was assumed in both calculations). We would then be justified in applying the empirically derived scaling of section 3.3 to extrapolate from JET to ITER conditions, which leads to an estimate of the ITER power width of 2.2-4.4 mm-omp, based on the empirical $\lambda_{q,int}$ scaling of section 3.3. A note of caution may well be added at this point: it was not possible nor was it intended within the context of the present paper to offer a critical review of power deposition profiles in other tokamaks (narrow profiles of the kind observed at JET have been reported on at least two other machines, C-Mod and Textor). Hence, the extrapolation from JET to ITER is made exclusively on the basis of the present findings. In addition, the impact of energetic ions on the divertor heat load is likely to be mitigated in ITER by the dense cloud of atomic hydrogen in the highly closed, V-shaped divertor leg. ASCOT simulations for ITER are planned to assess this point quantitatively.

5. CONCLUSIONS

The narrow feature in the power deposition profile, first observed in Ref.3, was confirmed by the swept strike-point thermocouple technique. The profile width was found to decrease with input power and increase with separatrix density according to $\lambda_{q,int} \propto P_{SOL}^{-0.4\pm0.1} n_{sep}^{+0.4\pm0.1}$, in constrast with the ITER-99 scaling which indicates a positive power dependence. The new scaling predicts a much narrower power width in ITER ($\lambda_{q,int} \sim 2.2$ - 4.4 mm-omp vs. ~15 mm-omp), although the higher plasma/neutral density (due to increased closure) in the ITER divertor is likely to broaden

the profile significantly. Decompostion of the deposited heat load into the ion and electron channels, the latter obtained from target Langmuir probes, revealed a strong correlation between the narrow layer and the ion component. Numerical modelling (ASCOT-OSM2/EIRENE) indicates that ion orbit losses from the pedestal-separatrix region are a probable cause of the observed narrow layer. The predicted ion deposition profile was found to match the measured profile (both in peak heat flux and integral width) for a high power H-mode, assuming a large outward radial electric field in the SOL of ~ 60 kV/m, which is however within the estimated range (no direct measurements of $E_{r,SOL}$ are available on JET at present). Further ASCOT simulations are currently underway and will be reported on shortly. Based on upstream collisionality ($\nu^{*}_{i,sep} \sim 0.5\text{-}1$), ion orbit losses are likely to play an important role in ITER SOL and divertor physics.

This work was conducted under European Fusion Development Agreement and was partly funded by EURATOM and the UK Department of Trade and Industry.

REFERENCES

[1]. ITER database, many authors, *Nuclear Fusion*, **39** (1999), 2423.

[2]. A.Loarte, "Multi-machine scaling of the divertor peak heat flux and width for L-mode and H-mode discharges", *J. Nucl. Materials*, **266-269** (1999), 99.

[3]. G.F.Matthews et al., "Divertor Energy Distribution in JET H-modes", *J. Nucl. Materials*, **290-293** (2001), 668.

[4]. V.Riccardo et al., "Reconstruction of power deposition profiles using JET MkIIGB thermocouple data for ELMy H-mode plasmas", *Plasma Phys. Contr. Fusion*, **43** (2001), 1.

[5]. R.D.Monk, "Langmuir Probe Measurements in the Divertor Plasma of the JET tokamak", Ph.D. Thesis, Imperial College London (1996).

[6]. P.C.Stangeby, The Plasma Boundary of Magnetic Fusion Devices, IoP Publishing, 2000.

[7]. T.Eich et al., "Analysis of Power deposition in JET MkIIGB divertor by IR-thermography", 28th EPS Conference on Controlled Fusion and Plasma Physics, Madeira, Portugal, 18-22 June 2001.

[8]. S.J.Davies, et al., "Behaviour of Upstream Separatrix Density in JET H-mode Plasmas",

[9]. ITER-FEAT - outline design report, ROM 19/01/00, ITER Meeting, Tokyo, January 2000.

[10]. W.Fundamenski, "Tokamak Edge Plasma Modelling Using an Improved Onion-Skin Method", Ph.D. Thesis, U.Toronto (1999).

[11]. O'Brien et al., *Nuclear Fusion* **32** (1992) 1351.

[12]. R. Simonini et al., *Cont. Plasma Physics,* **34** (1994) 347.

[13]. D.Reiter, *J.Nucl. Materials,* **196-198** (1992), 80.

[14]. W.Fundamenski, *J. Nucl. Materials*, **290-293** (2001), 593.

[15]. A.V.Chankin, G.M.McCracken, "Loss Ion Orbits at the Tokamak Edge", Nuclear Fusion, **33** (1993), 1459.

[16]. J.A.Heikkinen, Phys.Plasma, **8** (2001), 2824.

[17]. T. Kurki-Sounio et al., "Monte Carlo Simulations of the Heat Load Asymmetries on JET Divertor Plates", submitted to Nuclear Fusion (2001).

[18]. J.Lingertat, "Studies of giant ELM interaction with the divertor target in JET", *J. Nucl. Materials*, **241-243** (1997), 402.

[19]. Yu.Igitkhanov, "Physics Picture of Type I ELMs", 28th EPS Conference on Controlled Fusion and Plasma Physics, Madeira, Portugal, 18-22 June 2001.

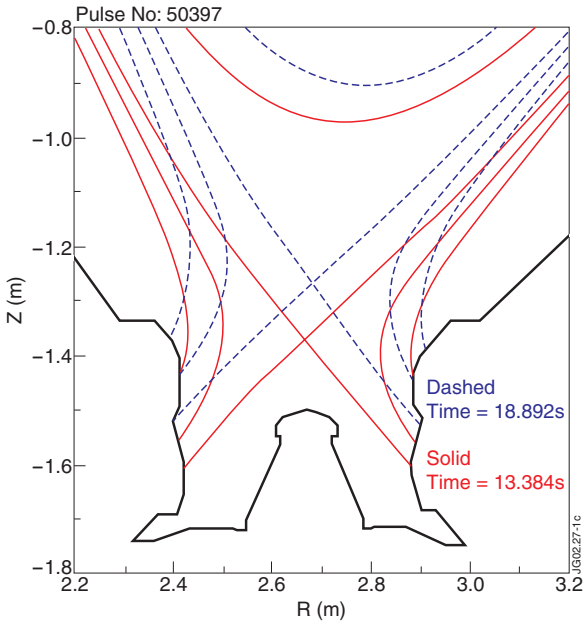

Figure 1: MkIIGB divertor target module. The orientation of the module with respect to the torus is indicated by the co-ordinate system: ϕ toroidal, θ poloidal. The perpendicular $\perp$ co-ordinate indicates the direction normal to the tile surface.

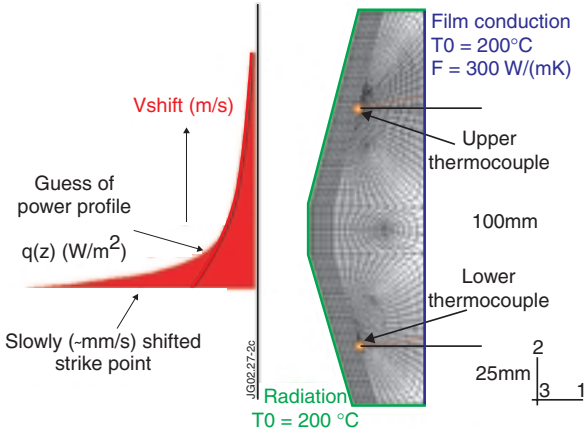

Figure 2: Initial and final positions of the vertical equilibrium sweep used in the TC method. The thermocouple used for the analysis is located roughly midway between these two positions.

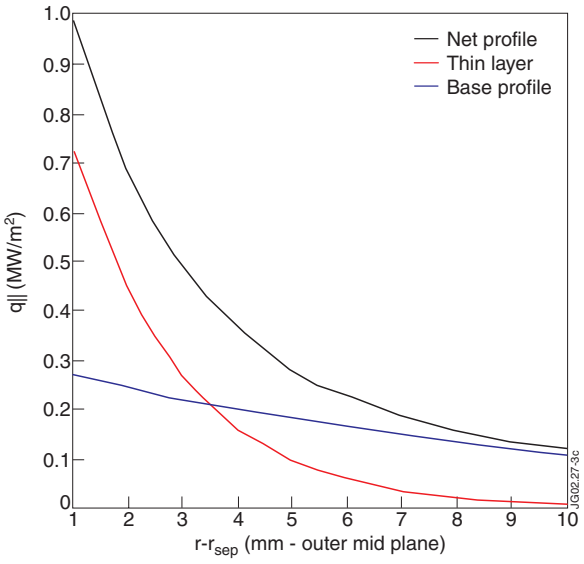

Figure 3: Finite element model of the outer vertical tile. The two thermocouples are located 25 and 125 mm above the bottom end of the tile and ~ 10 mm behind the plasma facing surface. The heat flux profile (perpendicular to the z-axis) and the thermal boundary conditions used in the simulations are shown schematically.

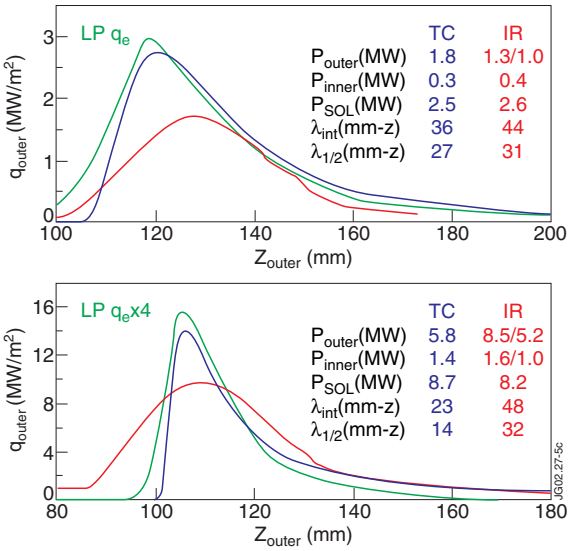

Figure.4: Double-exponential power profile used in the TC simulations, decomposed into the thin (T) and wide (W) components.

Figure 5: Langmuir probe radial profiles (mapped to the outer mid-plane) of plasma flux (Γ_0), electron temperature (T_e), and electron power $q_{||e}$ on the outer target for shot 50401 (12 MW NBI, H-mode). The vertical spikes indicate the presence of ELMs, while the lower envelope corresponds to the inter-ELM profile.

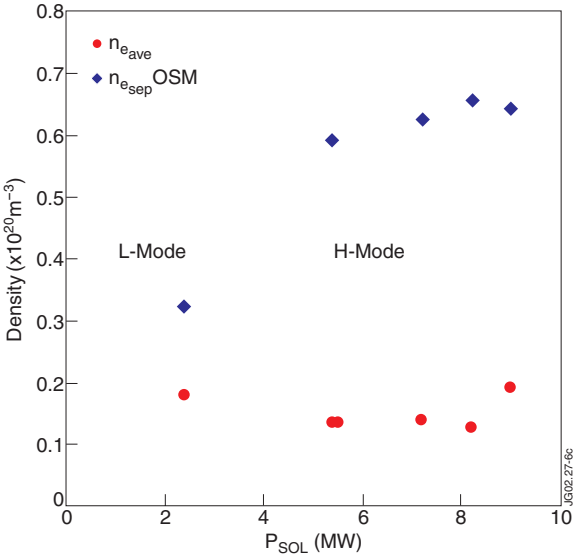

Figure 6: Comparison of Langmuir probe (LP, e) and Thermocouple (TC, tot) power deposition profiles at the outer target for a 4 MW L-mode (top) and 16 MW H-mode (bottom). The LP profiles correspond the lower envelope in Fig.5, while TC profiles are based on a best fit using a skewed gaussian trial function.

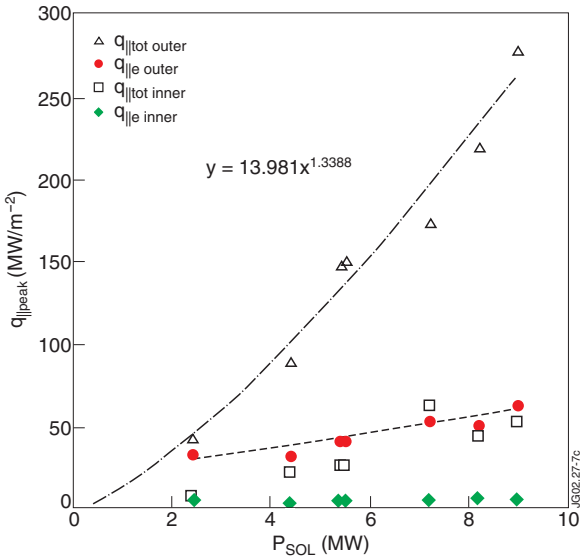

Figure 7: Core line-average and separatrix (OSM2/EIRENE) densities vs. power entering the scrape-off layer (SOL). Greenwald density in all cases ~ 1.0e20 m^{-3}.

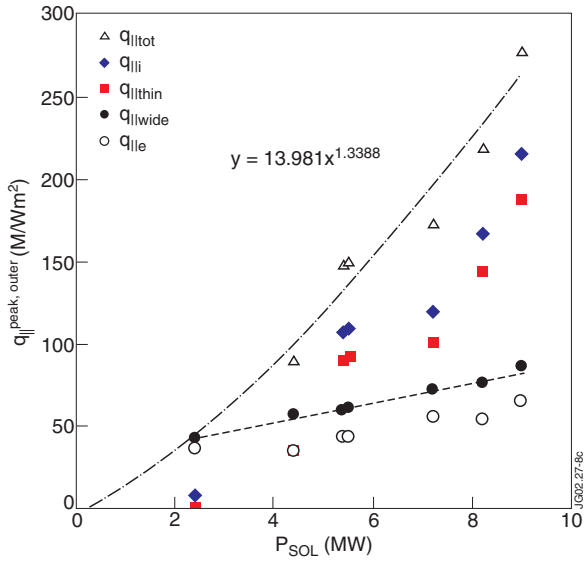

Figure 8: Peak parallel heat fluxes (total from TC, electron from LP) at both the outer and inner targets vs. power entering the SOL.

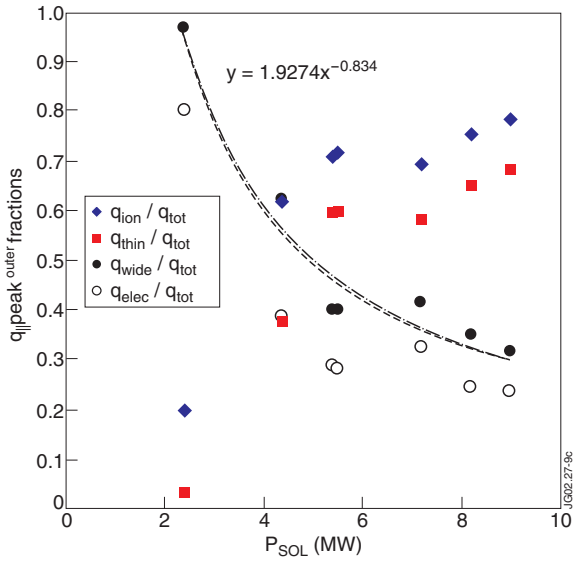

Figure 9: Peak parallel heat flux at the outer target broken down into the wide and thin components of the double-exponential profile, as well as the ion and electron channels. The results are plotted vs. power reaching the outer target (from TC analysis).

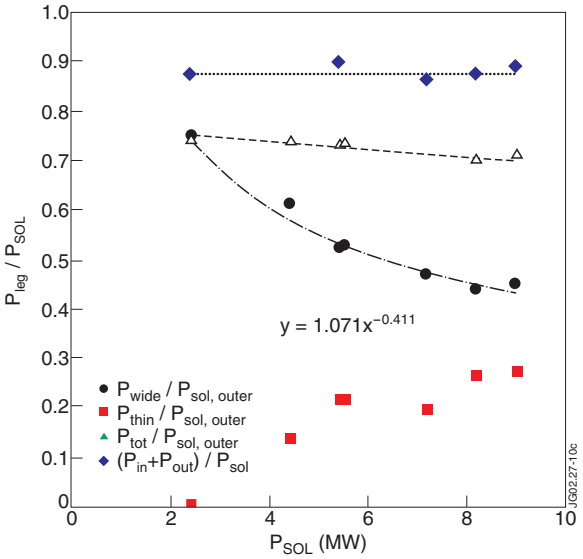

Figure 10: Results of Figure 9 expressed as fractions of the total parallel heat flux.

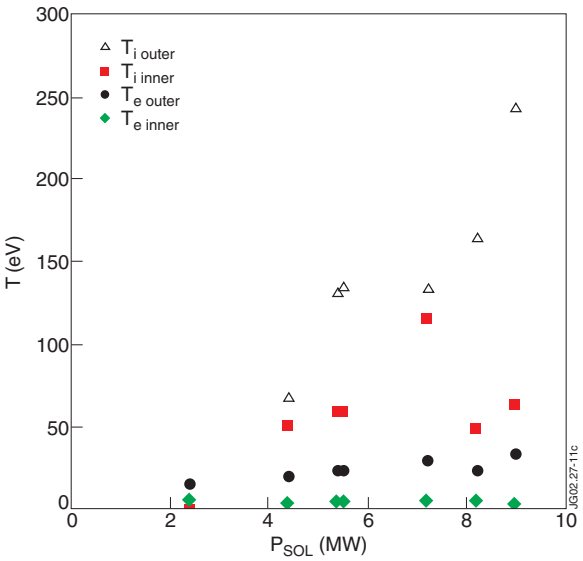

Figure 11: Total power deposited on the outer target, broken down into the thin and wide contributions, and the total power to both targets plotted vs. power entering the SOL.

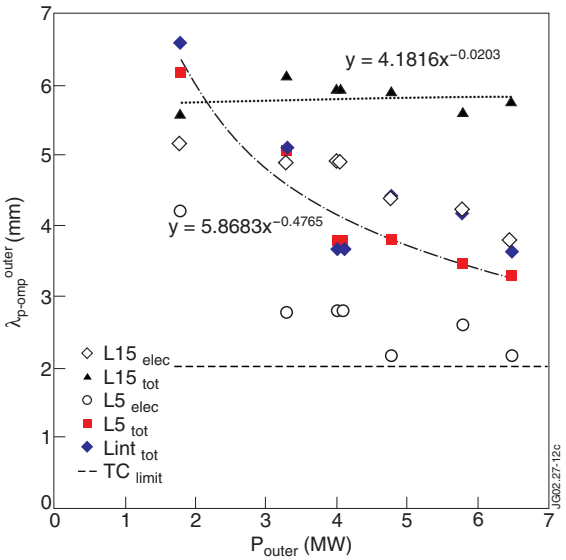

Figure 12: Electron and ion temperatures at the outer and inner targets vs. power entering the SOL.

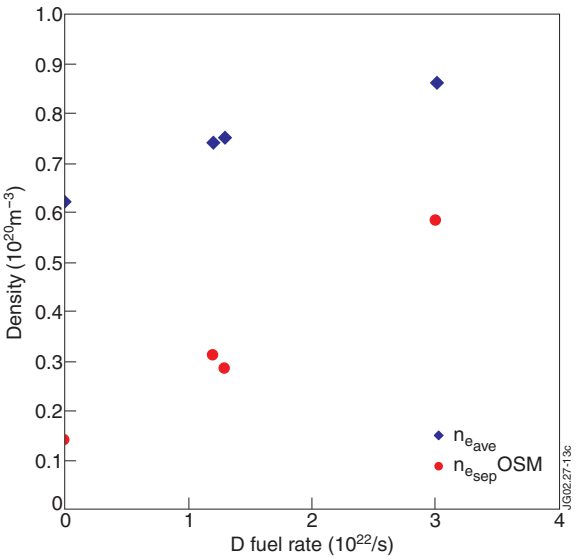

Figure 13: Characteristic outer target power profile widths mapped to the outer mid-plane (omp), integral width, and exponential widths fitted over the first 5 and 15 mm-omp, plotted vs. power entering the SOL.

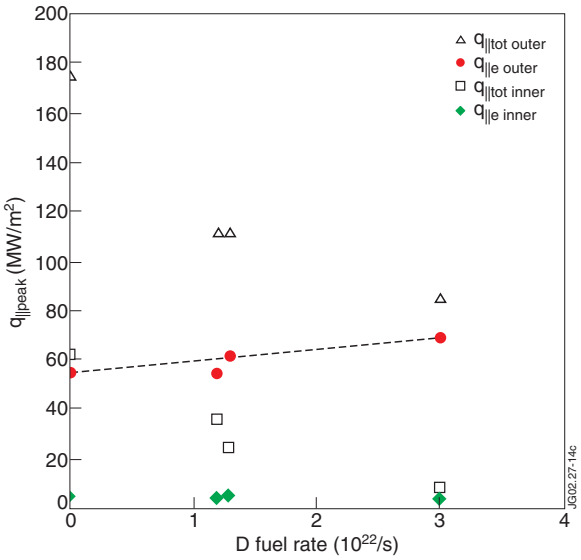

Figure 14: Core line-average and separatrix (OSM2/ EIRENE) densities vs. deuterium fuelling rate at constant NBI heating power.

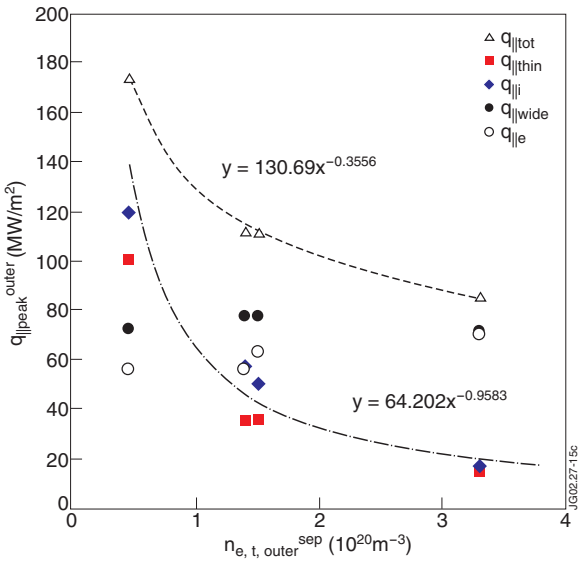

Figure 15: Peak parallel heat fluxes (total from TC, electron from LP) at both the outer and inner targets vs. D fuelling rate.

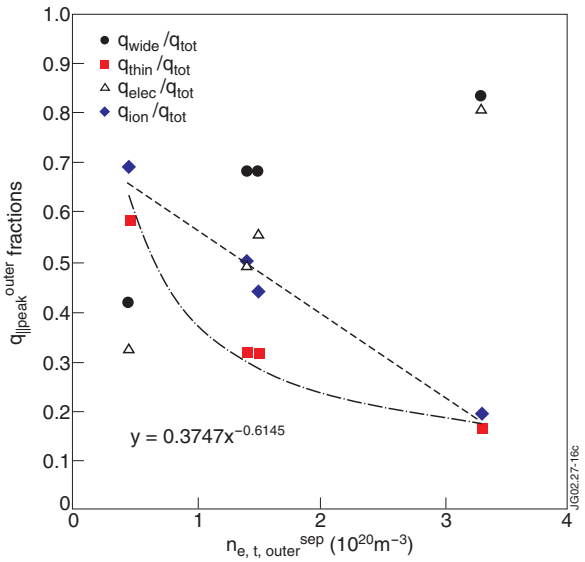

Figure 16: Peak parallel heat flux at the outer target broken down into the wide and thin components of the double-exponential profile, as well as the ion and electron channels. The results are plotted vs. electron density at the outer strike point.

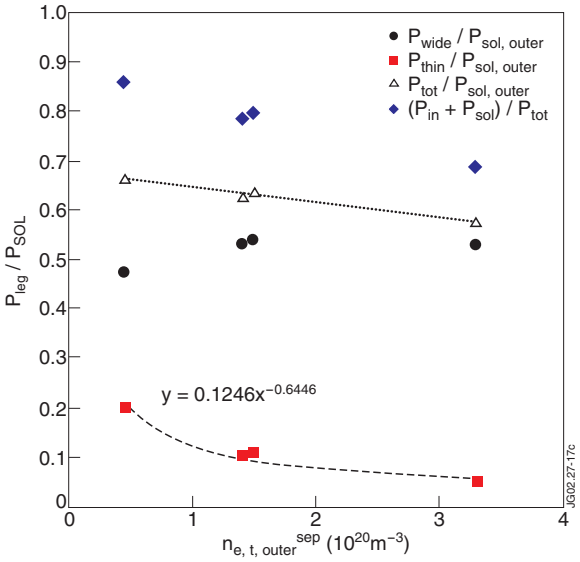

Figure 17: Results of Fig.16 expressed as fractions of the total parallel heat flux.

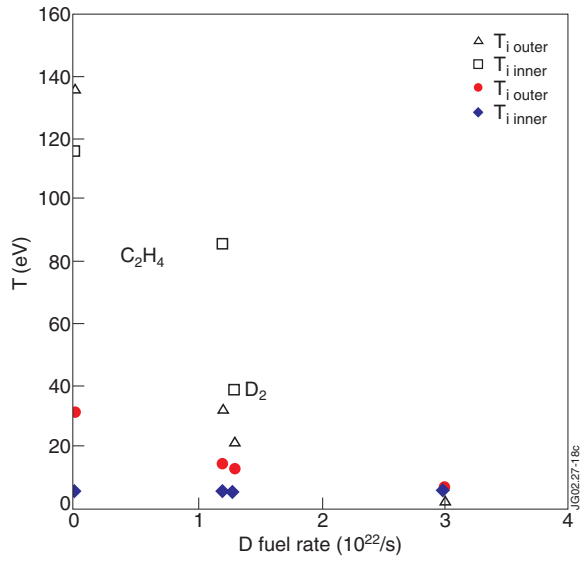

Figure 18: Total power deposited on the outer target, broken down into the thin and wide contributions, and the total power to both targets plotted vs. electron density at the outer strike point.

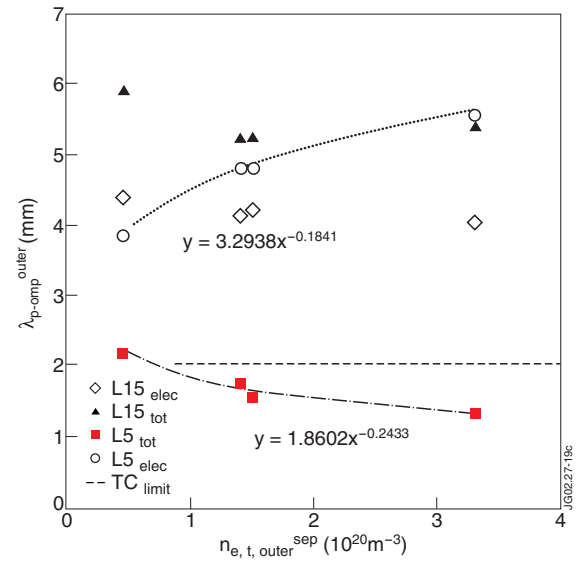

Figure 19: Electron and ion temperatures at the outer and inner targets vs. D fuelling rate. The fuelling species are indicated beside each group of four vertical points.

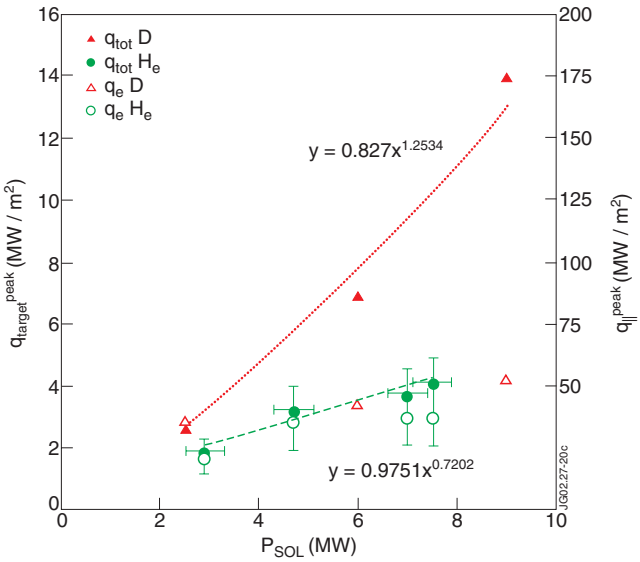

Figure 20: Characteristic outer target power profile widths mapped to the outer mid-plane (omp): integral width, and exponential widths fitted over the first 5 and 15 mm-omp plotted vs. electron density at the outer strike point.

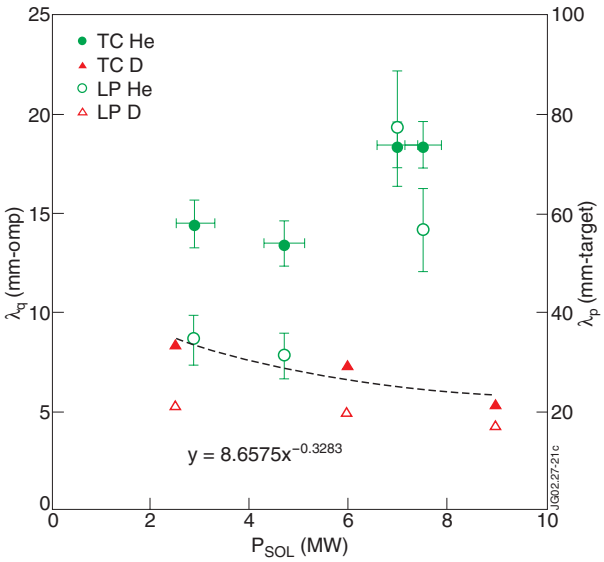

Figure 21: Comparison of the observed power decay length scaling ($\lambda_q \propto P^{\alpha} n^{\beta}$) with predictions of several theories of cross-field SOL transport. Since each model predicts one pair of power and density exponents (α,β), it is represented on the α vs.β plot by a single point. The two shaded regions indicate the empirically obtained scalings (with estimated uncertainties) with pedestal and separatrix densities and power entering the SOL.

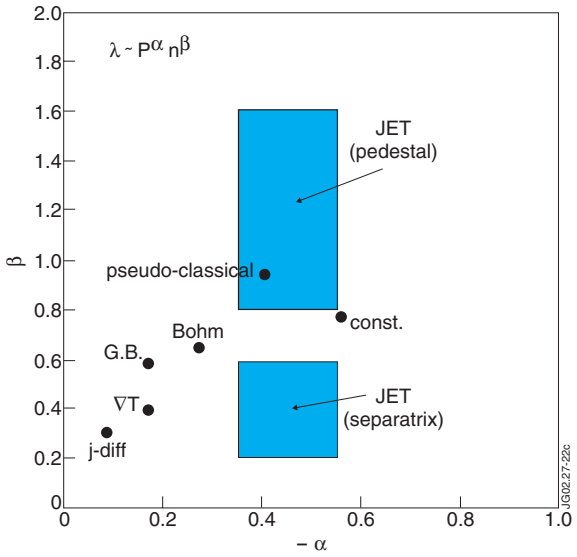

Figure 22: Radial profiles of ion and electron collisionalities for two different OSM2/EIRENE simulations of the shot-by-shot experiment (49511): the ratio of ion to electron power, P_i/P_e = 1 and 10.

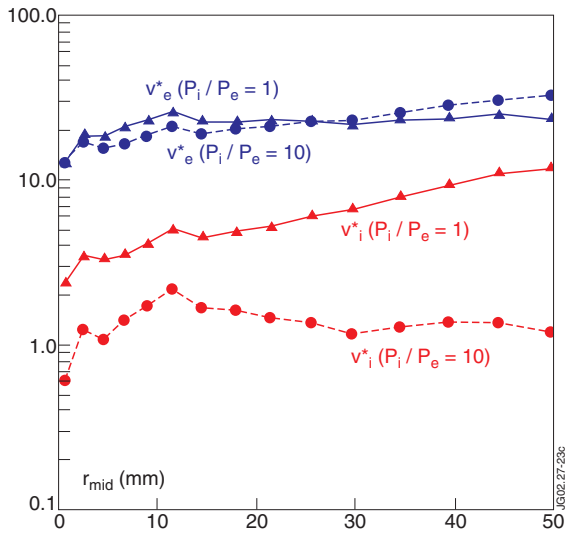

Figure 23: Radial profiles of ion and electron radial transport coefficients extracted using the onion-skin method from the simulations, compared with Bohm and neo-classical predictions.

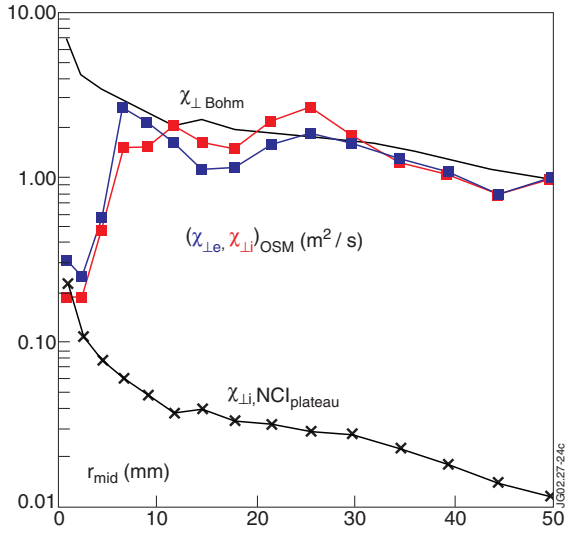

Figure 24: Poloidal distribution of local ion-ion collisionality (top) and ion-atom charge-exchange collisionality (bottom) based on OSM2/EIRENE simulation of 49511.

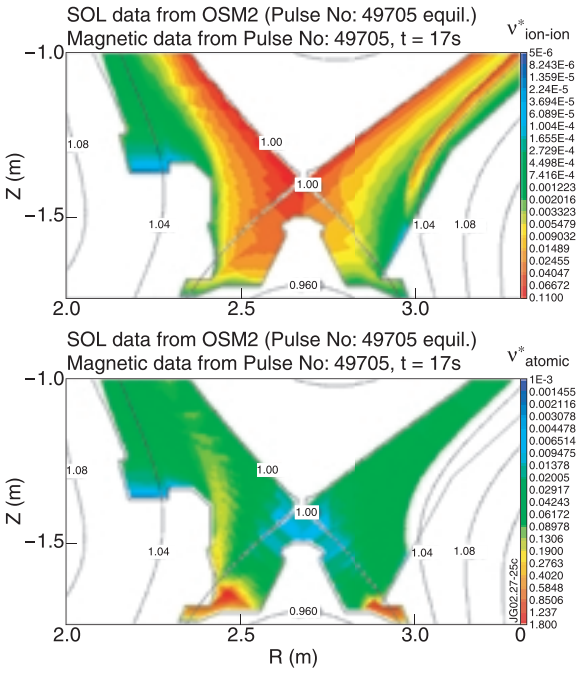

Figure 25: Loss regions in energy-angle phase space for ion orbit loss to the inner (shaded) and outer (clear) targets for three launch positions: outer mid-plane, inner mid-plane and X-point (downward B×∇B in all cases). Loss to outer/inner target dominates for ions launched from the outer/inner-mid plane.

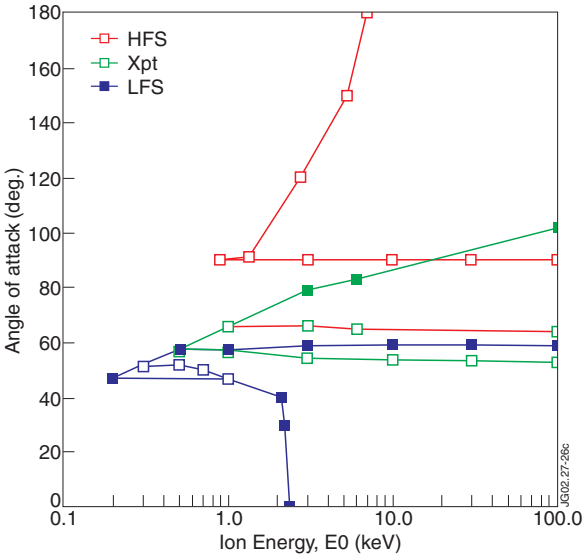

Figure 26: Ion orbit loss topologies for B×∇B ↓ (left) and ↑ (right) for ions originating at the outer and inner mid-planes, in the absence of collisions and electric fields. In the normal field direction (B×∇B ↓) ions are lost preferentially to the inner target.

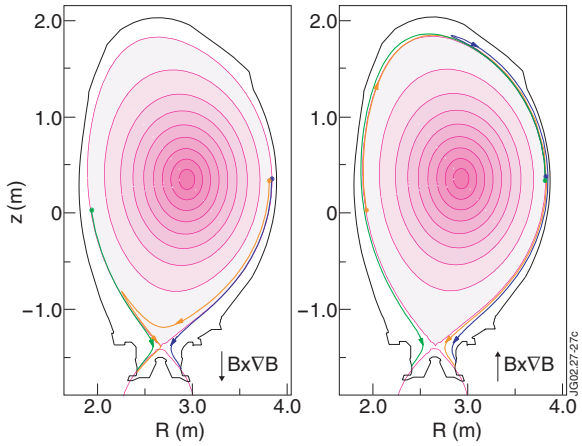

Figure 27: In-out ion orbit loss asymmetry in the normal field direction (B×∇B ↓) and with no electric fields, based on ASCOT trace calculations, plotted vs. ion pedestal collisionality.

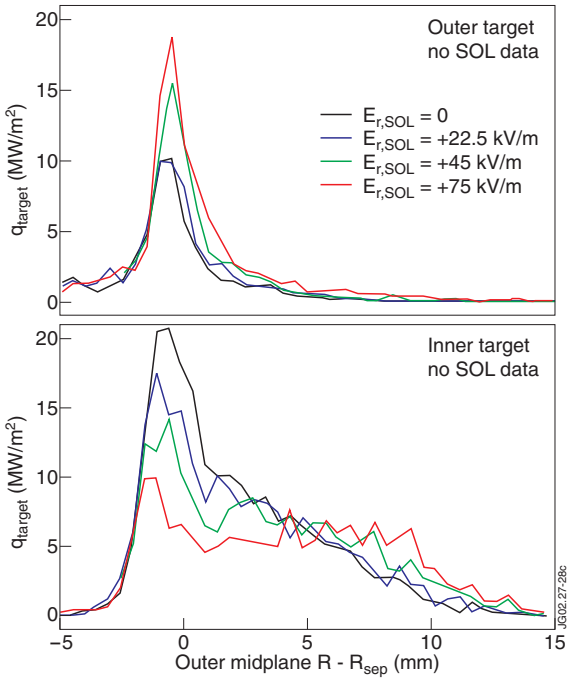

Figure 28: Ion loss power deposition profiles mapped to the outer mid-plane, for the outer target (top) and inner target (bottom), predicted by ASCOT for shot 49511 with no SOL plasma/neutrals and four levels of radial electric field in the SOL. The peak is slightly shifted below the magnetic strike point (~ 1 mm-omp) due to the downward B×∇B drift.

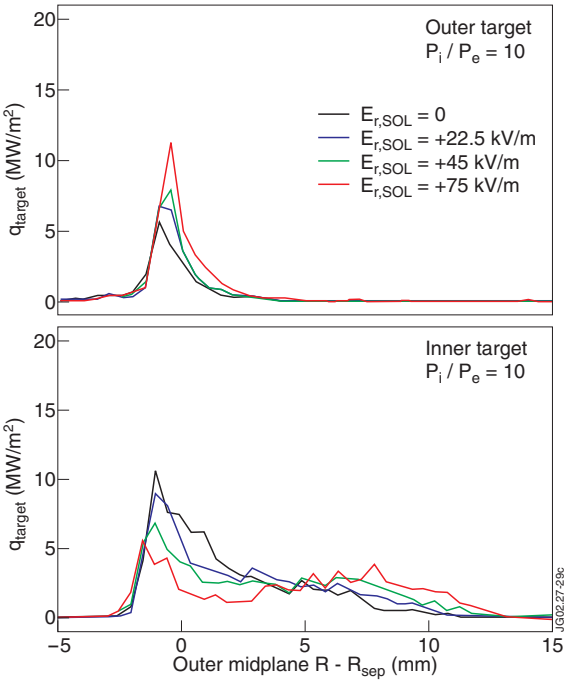

Figure 29: Same as Fig.28 but with OSM2/EIRENE background plasma/neutrals assuming P_i/P_e = 10.

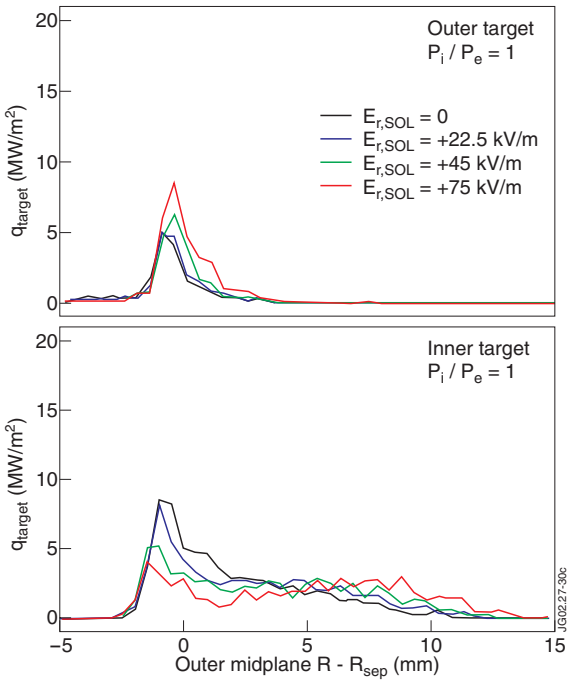

Figure 30: Same as Fig.28 but with OSM2/EIRENE background plasma/neutrals assuming P_i/P_e = 1.

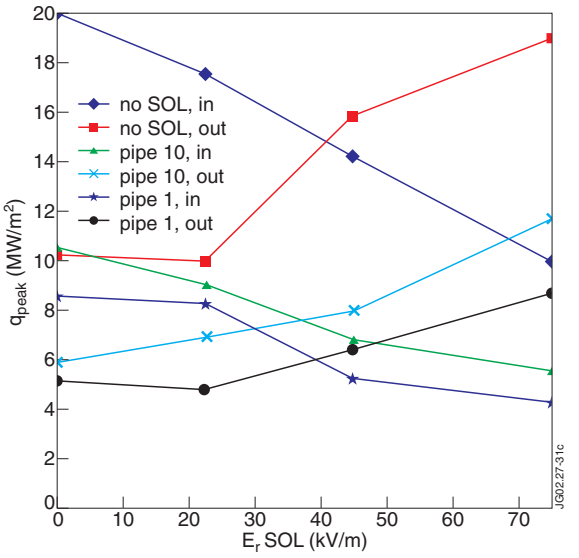

Figure 31: Peak ion heat flux predicted by ASCOT based on the results shown in Figs.28-30, plotted vs. the radial electric field in the SOL.

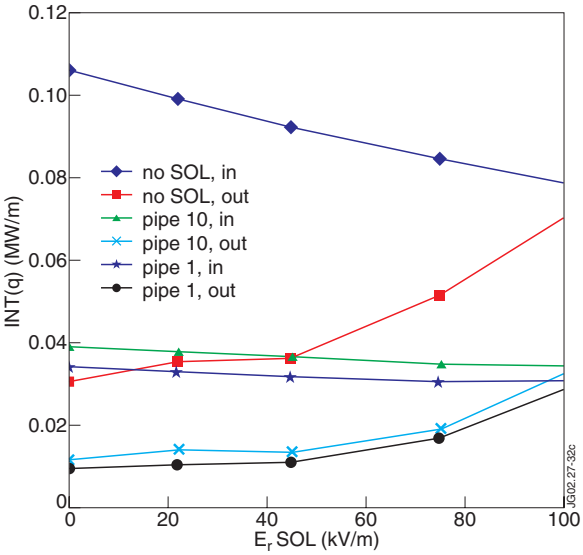

Figure 32: The integrated ion loss power predicted by ASCOT plotted vs. the radial electric field in the SOL.

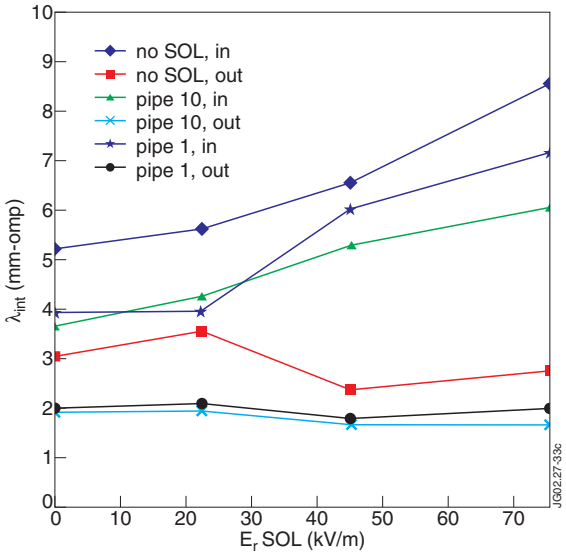

Figure 33: The integral profile widths predicted by ASCOT vs. the radial electric field in the SOL.

Table1: Comparison of six OSM2/EIRENE simulations of five JET discharges; numerical results, followed by an asterix (*), are intermixed with diagnostic data.

	49511	**49511**	**50401**	**50421**	**50404**	**50414**
OSM2 P_i/P_e [-]*	1	10	1	1	1	1
P_{NBI}[MW]	14	14	12	16	12	4
$\Gamma_D[10^{22}\ s^{-1}]$	0	0	0	0	3.0	0.5-1.5
mode, f_{ELM} [Hz]	H-I, 13	H-I, 13	H-I, 10	H-I, 15	H-I, 35	L
P_{SOL}[MW]	9.5	9.5	7.2	9.0	5.6	2.5
P_{outer}^{TC}[MW]	5.4	5.4	4.8	6.5	3.2	1.8
$P_{outer}^{OSM/LP}$[MW]	1.4	4.5	1.6	2.8	2.2	1.9
$q_{\|\|tot}^{peak}[MW/m^2]$	200	200	176	280	87	45
λ_5[mm-omp]	4	4	3.9	3.4	5.6	6.25
$T_{e,t,outer}$[eV]	31	32	25	35	9	16
$T_{e,sep}$[eV]*	70	70	87	100	108	69
$T_{e,ped}$[keV]	1.4	1.4	1.5	1.4	0.5	0.4
$T_{e,0}$[keV]	4.3	4.3	4.5	4.6	2.9	2.9
$T_{i,t,outer}$[eV]*	44	280	42	72	10	18
$T_{i,sep}$[eV]*	156	325	220	260	273	161
$n_{e,t,outer}[10^{19}\ m^{-3}]$	2.8	1.2	4.5	4.5	33.0	8.0
$n_{e,sep}[10^{19}m^{-3}]$*	1.0	1.0	1.4	1.9	5.8	1.8
$n_{e,ped}[10^{19}\ m^{-3}]$	2.5	2.5	2.5	2.5	5.4	2.1
$<n_e>[10^{19}\ m^{-3}]$	6.6	6.6	6.3	6.5	8.7	3.3
$\lambda_{ii,t,outer}$[m]*	0.66	63	0.38	1.11	0.0033	0.039
$\lambda_{ii,sep}$[m]*	23.5	101	33.3	34.3	12.4	13.9
$\lambda_{ii,ped}$[m]	756	756	868	756	44	73
$L_{\|\|}/2$[m]	50	50	50	50	50	50
$\lambda_{ee,t,outer}$[m]	0.33	0.81	0.13	0.26	0.0023	0.031
$\lambda_{ee,sep}$[m]*	4.57	4.57	5.18	5.05	1.93	2.53
$\lambda_{ee,ped}$[m]	752	752	863	752	44	73

Table 2: Results of ASCOT trace simulations of JET shot 49511 showing fractional ion loss and average ion energy to each target and the level of in-out asymmetry.

	f_{in} [%]	f_{out} [%]	E_{in} [keV]	E_{out} [keV]	f_{in}/f_{out}	E_{in}/E_{out}
Default	20.1	8.7	1.365	0.937	2.31	1.45
B×∇B↑	1.7	27.8	0.365	1.365	0.061	0.27
ρ=0.97	39.0	17.1	1.276	0.985	2.28	1.29
ρ=0.99	60.8	20.2	1.001	0.845	3.01	1.18
ρ=0.996	51.4	34.1	0.995	0.821	1.51	1.21
ρ=0.999	39.8	50.8	0.993	0.802	0.77	1.23
ρ=1.0	38.7	51.3	0.989	0.763	0.75	1.29
θ = (0,2π)	21.3	7.6	1.350	0.941	2.80	1.43
$n_{e,ped}=3\times10^{18}m^{-3}$	8.1	2.6	1.45	1.33	3.11	1.09
$n_{e,ped}=3\times10^{19}m^{-3}$	36.5	12.3	1.372	0.868	2.97	1.58
$n_{e,ped}=10^{20}m^{-3}$	42.9	26.0	1.411	1.01	1.65	1.40
$n_{e,ped}=3\times10^{20}m^{-3}$	41.8	48.4	1.034	1.026	0.86	1.01
$T_{i,ped}$=100 eV	9.9	10.2	0.12	0.091	0.97	1.32
$T_{i,ped}$=300 eV	18.2	10.4	0.34	0.255	1.75	1.33
$T_{i,ped}$=3 keV	25.7	5.5	4.57	2.95	4.67	1.55

Table 3: Results of ASCOT trace simulations of JET shot 49511 with three different SOL backgrounds.

	f_{in}[%] $P_i/P_e = 10$	f_{out}[%] $P_i/P_e = 10$	f_{in}/f_{out} no SOL	f_{in}/f_{out} $P_i/P_e = 10$	E_{in}/E_{out} no SOL	E_{in}/E_{out} $P_i/P_e = 10$
Default	19.7	9.0	2.42	2.19	1.34	1.56
B×∇B↑	3.8	23.7	0.17	0.16	0.60	0.77
$E_i = 0.5T_i$	17.3	9.3	1.86	1.85	1.13	1.49
$E_i = 4.5T_i$	18.5	10.2	1.76	1.81	1.42	1.31
E_r^{core} = - 50 kV/m	19.7	9.0	1.87	2.19	1.08	1.56
E_r^{core} = + 100 kV/m	61.6	37.0	2.06	1.66	1.55	2.65
E_r^{SOL} = - 100 kV/m	23.5	4.2	3.21	5.58	0.88	0.93
E_r^{SOL} = + 100 kV/m	5.9	23.3	0.86	0.25	2.0	4.42

Table 4: Comparison of key parameters relevant to power exhaust for JET shot 50421 and the ITER reference scenario, both with $P_i/P_e = 1$.

	JET	**ITER**	**ITER/JET**
R [m]	3.0	6.2	2.1
B [T]	2.4	5.3	2.2
I_p [MA]	2.5	15	6.0
q_{95}	2.7	3.0	1.1
P_{SOL} [MW]	9.0	75	7.5
$<n_e>[10^{19}\ m^{-3}]$	6.5	10	1.55
$n_{e,sep}[10^{19}m^{-3}]$	1.9	3.0	1.56
$T_{e,sep}$[eV]	100	200	2.0
$T_{i,sep}$[eV]	260	400	1.5
$\nu^*_{e,\,sep}$	9.9	4.8	0.48
$\nu^*_{i,\,isep}$	1.45	1.1	0.75